

# Surveys in Geophysics

## Observational Assessment of Changes in Earth's Energy Imbalance Since 2000

--Manuscript Draft--

<b>Manuscript Number:</b>	GEOP-D-23-00138R2	
<b>Full Title:</b>	Observational Assessment of Changes in Earth's Energy Imbalance Since 2000	
<b>Article Type:</b>	Review Paper	
<b>Keywords:</b>	Earth's Energy Imbalance; Climate Change; Clouds; Satellite; Earth Radiation Budget	
<b>Corresponding Author:</b>	Richard P. Allan : University of Reading Department of Meteorology Reading, Berks UNITED KINGDOM OF GREAT BRITAIN AND NORTHERN IRELAND	
<b>Corresponding Author Secondary Information:</b>		
<b>Corresponding Author's Institution:</b>	: University of Reading Department of Meteorology	
<b>Corresponding Author's Secondary Institution:</b>		
<b>First Author:</b>	Norman Loeb	
<b>First Author Secondary Information:</b>		
<b>Order of Authors:</b>	Norman Loeb	
	Seung-Hee Ham	
	Richard Allan	
	Tyler Thorsen	
	Benoit Meyssignac	
	Seiji Kato	
	Gregory Johnson	
	John Lyman	
<b>Order of Authors Secondary Information:</b>		
<b>Funding Information:</b>	Research Councils UK (NE/RO16518/1)	Dr. Richard Allan
<b>Abstract:</b>	<p>Observations from the Clouds and the Earth's Radiant Energy System (CERES) show that Earth's energy imbalance (EEI) has doubled from <math>0.5 \pm 0.2</math> <math>\text{Wm}^{-2}</math> during the first 10 years of this century to <math>1.0 \pm 0.2</math> <math>\text{Wm}^{-2}</math> during the past decade. The increase is the result of a <math>0.9 \pm 0.3</math> <math>\text{Wm}^{-2}</math> increase absorbed solar radiation (ASR) that is partially offset by a <math>0.4 \pm 0.25</math> <math>\text{Wm}^{-2}</math> increase in outgoing longwave radiation (OLR). Despite marked differences in ASR and OLR trends during the hiatus, transition-to-El Niño and post-El Niño periods, trends in net top-of-atmosphere (TOA) flux (NET) remain within <math>0.1</math> <math>\text{Wm}^{-2}</math> per decade of one another, implying a steady acceleration of climate warming. Northern and southern hemisphere trends in NET are consistent to <math>0.06 \pm 0.31</math> <math>\text{Wm}^{-2}</math> per decade due to a compensation between weak ASR and OLR hemispheric trend differences of opposite sign. We find that large decreases in stratocumulus and middle clouds over the subtropics and decreases in low and middle clouds at mid-latitudes are the primary reasons for increasing ASR trends in the northern hemisphere (NH). These changes are especially large over the eastern and northern Pacific Ocean, and coincide with large increases in sea-surface temperature (SST). The decrease in cloud fraction and higher SSTs over the NH subtropics lead to a significant increase in OLR from cloud-free regions, which partially compensate for the NH ASR increase. Decreases in middle cloud reflection and a weaker reduction in low cloud reflection account for the increase in ASR in the southern hemisphere, while OLR changes are weak.</p>	

**Response to Reviewers:**

Keywords are added at the end of the Abstract and three Article Highlights follow these immediately as requested. Thank you for your assistance with this manuscript.

1           **Observational Assessment of Changes in Earth's Energy Imbalance Since 2000**

2  
3       Norman G. Loeb<sup>1</sup>, Seung-Hee Ham<sup>2</sup>, Richard P. Allan<sup>3</sup>, Tyler J. Thorsen<sup>1</sup>, Benoit Meyssignac<sup>4</sup>,  
4                                       Seiji Kato<sup>1</sup>, Gregory C. Johnson<sup>5</sup>, John M. Lyman<sup>5,6</sup>

5  
6       <sup>1</sup>*NASA Langley Research Center, Hampton, Virginia, USA*

7       <sup>2</sup>*Analytical Mechanics Associates (AMA), Hampton, USA*

8       <sup>3</sup>*Department of Meteorology and National Centre for Earth Observation, University of Reading,*  
9       *Reading, UK*

10      <sup>4</sup>*LEGOS, Université de Toulouse, CNES, CNRS, UPS, IRD, Toulouse, France*

11      <sup>5</sup>*NOAA/Pacific Marine Environmental Laboratory, Seattle, Washington, USA*

12      <sup>6</sup>*CIMAR, University of Hawaii, Honolulu, Hawaii, USA*

13  
14  
15  
16  
17      Submitted to: *Surveys in Geophysics* special issue: *Earth's Changing Water and Energy Cycle*

18

19 **Abstract** Observations from the Clouds and the Earth's Radiant Energy System (CERES) show  
20 that Earth's energy imbalance (EEI) has doubled from  $0.5\pm 0.2 \text{ Wm}^{-2}$  during the first 10 years of  
21 this century to  $1.0\pm 0.2 \text{ Wm}^{-2}$  during the past decade. The increase is the result of a  $0.9\pm 0.3 \text{ Wm}^{-2}$   
22 increase absorbed solar radiation (ASR) that is partially offset by a  $0.4\pm 0.25 \text{ Wm}^{-2}$  increase in  
23 outgoing longwave radiation (OLR). Despite marked differences in ASR and OLR trends during  
24 the hiatus, transition-to-El Niño and post-El Niño periods, trends in net top-of-atmosphere (TOA)  
25 flux (NET) remain within  $0.1 \text{ Wm}^{-2}$  per decade of one another, implying a steady acceleration of  
26 climate warming. Northern and southern hemisphere trends in NET are consistent to  $0.06\pm 0.31$   
27  $\text{Wm}^{-2}$  per decade due to a compensation between weak ASR and OLR hemispheric trend  
28 differences of opposite sign. We find that large decreases in stratocumulus and middle clouds over  
29 the subtropics and decreases in low and middle clouds at mid-latitudes are the primary reasons for  
30 increasing ASR trends in the northern hemisphere (NH). These changes are especially large over  
31 the eastern and northern Pacific Ocean, and coincide with large increases in sea-surface  
32 temperature (SST). The decrease in cloud fraction and higher SSTs over the NH subtropics lead  
33 to a significant increase in OLR from cloud-free regions, which partially compensate for the NH  
34 ASR increase. Decreases in middle cloud reflection and a weaker reduction in low cloud reflection  
35 account for the increase in ASR in the southern hemisphere, while OLR changes are weak.

36

37

38

39

40

41 **Article Highlights**

- 42 • Satellite observations reveal that global mean net flux (NET) at the top-of-atmosphere (or  
43 equivalently, Earth’s energy imbalance) has doubled during the first twenty years of this  
44 century. The increase is associated with a marked increase in absorbed solar radiation  
45 (ASR) that is partially offset by an increase in outgoing longwave radiation (OLR)
- 46 • While ASR and OLR changes within sub-periods corresponding to the hiatus  
47 (03/2000–05/2010), transition-to-El Niño (06/2010-05/2016), and post-El Niño  
48 (06/2016–12/2022) vary substantially, NET flux changes are remarkably stable (within  
49  $0.1 \text{ Wm}^{-2}$  per decade), implying a steady acceleration of climate warming
- 50 • The increase in ASR is associated with decreases in stratocumulus and middle cloud  
51 fraction and reflection in the Northern Hemisphere, and decreases in middle cloud  
52 reflection in the Southern Hemisphere. The cloud changes are especially large in areas  
53 with marked increases in sea-surface temperature, such as over the eastern and northern  
54 Pacific Ocean
- 55 • Continued monitoring of Earth’s radiation budget and new and updated climate model  
56 simulations are critically needed to understand how and why Earth’s climate is changing  
57 at such an accelerated pace

58

59

60

61 **Keywords**

62 Earth’s Energy Imbalance; Climate Change; Clouds; Satellite; Earth Radiation Budget

63

## 64 **1. Introduction**

65 Earth's radiation budget (ERB) describes how radiant energy is exchanged between Earth  
66 and space and how it is distributed within the climate system. The balance between incoming solar  
67 radiant energy absorbed by Earth and outgoing thermal infrared radiation emitted to space (also  
68 called Earth's Energy Imbalance, or EEI) determines whether Earth heats up or cools down  
69 (Hansen et al., 2005; Trenberth et al., 2014). A positive EEI is concerning as the extra energy  
70 added to the climate system leads to warming of the oceans, land and atmosphere, sea level rise,  
71 melting of snow and ice, and shifts in atmospheric and oceanic circulations (von Schuckmann et  
72 al., 2016). Approximately 89% of this additional heat is stored in the ocean, while the rest warms  
73 the land (5%) and atmosphere (2%) and melts ice (4%) (von Schuckmann et al., 2023).

74 Multiple lines of evidence show that EEI is increasing. These include an in situ based Earth  
75 heat inventory that quantifies how much heat has accumulated in the Earth system and where the  
76 heat is stored (von Schuckmann et al., 2023; Minière et al., 2023; Li et al., 2023; Storto and Yang,  
77 2024; Cheng et al., 2024), satellite observations of top-of-atmosphere (TOA) radiative fluxes from  
78 the Clouds and the Earth's Radiant Energy System (CERES) (Loeb et al., 2021a), and satellite  
79 measurements of sea level and ocean mass change (Hakuba et al., 2021; Meyssignac et al., 2023;  
80 Marti et al., 2023). In situ based Earth heat inventory observations of global ocean heat content  
81 (OHC) and non-ocean components (atmosphere, land and cryosphere) indicate a robust  
82 acceleration of Earth system heating since 1960 (von Schuckmann et al., 2023; Minière et al.,  
83 2023; Li et al., 2023; Storto and Yang, 2024; Cheng et al., 2024). The acceleration rate for  
84 1960–2020 is  $0.15 \pm 0.05 \text{ Wm}^{-2} \text{ dec}^{-1}$  and  $0.30 \pm 0.28 \text{ Wm}^{-2} \text{ dec}^{-1}$  for the more recent period  
85 between 2002 and 2020 (Minière et al., 2024). The latter is consistent within uncertainty with  
86 satellite observations of TOA net flux (Loeb et al., 2021a; Loeb et al., 2022). In a comparison of

87 CERES EEI with 18 OHC products derived from in-situ, geodetic satellite observations, and ocean  
88 reanalyses for 2005-2019, Hakuba et al. (2024, this collection) show that while there is much  
89 spread in ocean heat uptake (OHU) and the rate of increase in OHU amongst the different analyses,  
90 the main reason for this spread is inadequate spatial-temporal sampling of the ocean. Datasets with  
91 better ocean coverage by filling in data sparse regions with satellite data or physical models  
92 (reanalyses) more closely match TOA net flux variability from CERES and show a positive trend  
93 in OHU that is similar in magnitude to CERES. It's worth noting that better sampling does not  
94 always guarantee better results. Loeb et al. (2022) argue that in the case of ocean reanalyses,  
95 achieving reliable temporal fidelity also depends upon model bias and whether new data are  
96 introduced/removed from the time series.

97 Few studies have examined what is driving the EEI increase since 2000. Raghuraman et  
98 al. (2021) used Coupled Model Intercomparison Project Phase 6 (CMIP6) (Eyring et al., 2016)  
99 simulations from the Geophysical Fluid Dynamics Laboratory Coupled/Atmospheric Model 4.0  
100 (GFDL CM4/AM4) (Zhao et al., 2018; Held et al., 2019) to assess the contributions of internal  
101 variability, effective radiative forcing (ERF) and climate feedbacks on the CERES trend. They  
102 conclude that the positive EEI trend can only be explained if the simulations account for the  
103 increase in anthropogenic radiative forcing and associated climate response since 2000. This is  
104 confirmed with four additional CMIP6 models by Hodnebrog et al. (2024), who further showed  
105 that effective radiative forcing due to anthropogenic aerosol emission reductions contributes  
106  $0.2 \pm 0.1 \text{ Wm}^{-2} \text{ dec}^{-1}$  to the trend in EEI. Kramer et al. (2021) used satellite data to infer  
107 instantaneous radiative forcing, providing observational evidence that radiative forcing is a major  
108 factor behind the EEI trend. Unfortunately, the number of assessments of the observed EEI trend  
109 are limited because the CMIP6 protocol ends in 2014. Schmidt et al. (2023) propose a new

110 atmosphere-only model intercomparison, CERESMIP, that targets the CERES period using  
111 updated sea-surface temperatures (SSTs), forcings and emissions through 2021. These new  
112 Atmospheric Model Intercomparison Project (AMIP) simulations will greatly expand the number  
113 of models available for model-observation comparisons and attribution studies of the EEI trend.

114 An observation-based partial radiative perturbation (PRP) analysis based upon the  
115 methodology of Thorsen et al. (2018) indicates that the CERES trend in EEI since 2000 is  
116 manifested in the data through changes in cloud, water vapor, trace gases, surface albedo and  
117 aerosols, which combine to increase TOA net downward radiation in excess of a negative  
118 contribution from increasing temperature (Loeb et al., 2021a). These changes are a consequence  
119 of the combined effects of climate forcing, feedback, and internal variability. To date, there has  
120 not been a thorough analysis of how different cloud types contribute to the observed changes in  
121 EEI. Loeb et al. (2021a) show that there is a large contribution by clouds to absorbed solar radiation  
122 changes and a weaker contribution to outgoing longwave radiation changes of opposite sign, but  
123 it does not attribute these to any particular cloud type. Furthermore, Loeb et al. (2021a) note  
124 substantial variations in TOA radiation during different sub-periods within the CERES record  
125 associated with internal variability.

126 In the following, we provide an observational assessment of TOA radiation changes that  
127 updates prior analyses by considering the period from 2000 to 2022 using CERES data products  
128 (Section 3.1). We examine the global, zonal and regional variations and trends in TOA radiation  
129 both for the entire CERES period and sub-periods corresponding to the hiatus, transition-to-El  
130 Nino, and post-El Nino to highlight TOA radiation changes across periods of markedly different  
131 internal variability (Section 3.2). We also use the new CERES FluxByCldTyp (FBCT) data  
132 product (Sun et al., 2022) to quantify the contribution to TOA radiation changes by different cloud



133 types using a cloud classification scheme based upon cloud types provided in FBCT (Section 3.3).  
134 Finally, we discuss some of the challenges associated with isolating the underlying processes that  
135 contribute to changes in TOA radiation from observations alone (Section 4).

## 136 **2. Data and Methods**

### 137 **2.1. TOA Radiation and Cloud Datasets**

138 Anomalies in TOA radiation components relative to their seasonal cycles are determined from  
139 the CERES Energy Balanced and Filled (EBAF) Ed4.2 product (Loeb et al., 2018) for  
140 03/2000–12/2022. The anomalies are determined by differencing the average in a given month  
141 from the average of all years of the same month. Throughout the paper, anomalies are defined  
142 positive downwards (hence the naming convention “–OLR” to indicate that an increase in OLR  
143 corresponds to a loss of energy relative to climatology). Trends are determined from monthly  
144 anomalies using least squares linear regression and uncertainties in the trends follow the approach  
145 described in Loeb et al. (2022). The EBAF product uses an objective constraint algorithm  
146 (Loeb et al., 2009) to adjust SW and LW TOA fluxes within their ranges of uncertainty to anchor  
147 global net TOA flux to an in situ estimate of the global mean EEI from mid-2005 to mid-2015  
148 (Johnson et al., 2016). Use of this approach to anchor the satellite-derived EEI does not impact the  
149 variability and trends in the data (Loeb et al., 2018). The EBAF product provides two clear-sky  
150 fluxes, one for cloud-free portions of a region and a second for the total region. The latter was  
151 introduced to provide an observation-based clear-sky flux defined in the same way as climate  
152 models (Loeb et al., 2020). Here we only consider clear-sky fluxes for cloud-free areas of a region  
153 and use that to compute cloud radiative effect (CRE), defined as the difference between all-sky  
154 and clear-sky downward TOA flux. Loeb et al. (2020) show that while the magnitudes of clear-

155 sky fluxes associated with the two definitions can be quite large, differences between their  
156 anomalies are relatively small.

157 TOA radiation changes for different cloud types are evaluated using the CERES  
158 FluxbyCldTyp Ed4.1-daily and -monthly products (Sun et al., 2022). The FBCT product has been  
159 used previously to generate observation-based cloud radiative kernels to quantify the sensitivity in  
160 TOA radiation to perturbations in meteorological conditions (Scott et al., 2020; Oreopoulos et al.,  
161 2022; Wall et al., 2022; Myers et al., 2023), to study changes in cloud properties and radiative  
162 fluxes by cloud type as a function of convective aggregation (Xu et al., 2023), and to evaluate  
163 climate models (Eitzen et al., 2017). FBCT provides CERES Terra and Aqua daytime 1°-regional  
164 gridded daily and monthly averaged TOA radiative fluxes and MODIS-derived cloud properties  
165 (Minnis et al. 2008, 2011a,b) stratified into 42 cloud types for 6 cloud optical depth and 7 cloud  
166 effective pressure intervals, as defined in Rossow and Schiffer (1991). The cloud types are defined  
167 from the vantage point of an observer in space that only sees the clouds that are exposed to space.  
168 Thus, cloud effective pressure is determined from the topmost portion of a cloudy column and  
169 optical depth corresponds to column optical depth (Cole et al., 2011). TOA fluxes are also provided  
170 for all-sky and clear-sky conditions. In FBCT, “clear-sky” corresponds to fractional area within a  
171 1°×1° region (gridbox hereafter) that is not covered by cloud. Since the FBCT uses Terra and  
172 Aqua, it only starts in July 2002 onwards. Accordingly, we consider 07/2002-12/2022 to assess  
173 changes in cloud fraction by cloud type.

## 174 **2.2. Changes in TOA Radiation by Cloud Class**

175 To assess the influence of cloud changes on TOA fluxes, we develop a cloud classification  
176 scheme using 1°×1° gridded daily mean Estimated Inversion Strength (EIS) parameter (Wood and  
177 Bretherton, 2006) provided in the SSF1deg Ed4.1-daily product (Doelling et al., 2013) and cloud

178 type information from the FBCT Ed4.1-daily and -monthly products (Sun et al., 2022). EIS is  
179 derived from surface pressure, temperature and dew point temperature at 2 m, and temperature and  
180 geopotential height at 700 hPa provided in the GEOS-DAS V5.4.1 product (Rienecker et al., 2008).

181 We first produce a gridded monthly EIS-by-cloud-type dataset from the SSF1deg Ed4.1-  
182 daily and FBCT Ed4.1-daily products by sorting gridded daily EIS values into the 42 FBCT cloud  
183 types in each gridbox each day and averaging these monthly. The monthly EIS-by-cloud-type data  
184 are then used together with the FBCT-monthly product to determine cloud fraction and TOA flux  
185 gridbox averages for three low cloud type classes equatorward of 60° (Table 1). The three low  
186 cloud classes have cloud effective pressures >680 hPa with EIS values >5 K Stratocumulus (Sc),  
187 0-5 K Stratocumulus-to-Cumulus Transition (SCT), and <0 K Cumulus (Cu). This EIS  
188 stratification of low clouds is an estimate based upon the regional distribution of annual mean EIS,  
189 SW CRE, SST and vertical velocity at 700 hPa (e.g., see Fig. 1 from Myers and Norris, 2015). In  
190 regions with EIS >5 K, SW CRE is strongly negative, indicating that the clouds are bright, SSTs  
191 are cooler than surrounding regions, and subsidence is appreciable. These characteristics are  
192 consistent with stratocumulus (Wood, 2012). Regions with EIS between 0 and 5 K exhibit weaker  
193 SW cloud radiative cooling, warmer SSTs, and weaker subsidence, consistent with stratocumulus-  
194 to-cumulus transition regimes. Low cloud areas with EIS <0 K primarily occur in the tropical trade  
195 wind region over warm oceans where shallow cumulus typically reside. Middle and high cloud  
196 classes equatorward of 60° are defined for cloud effective pressures of 440-680 hPa and <440 hPa,  
197 respectively. A polar cloud class is defined for all clouds poleward of 60°.

198 The regional distribution of the cloud classes in Table 1 for September 2002 (Fig. 1a-f)  
199 shows that three low cloud classes exhibit a smooth transition from Sc off the west coasts of the  
200 Americas and southern Africa to SCT mainly over the Southern Oceans and Cu mainly over the

201 tropics. Middle and high clouds are distributed throughout 60°S-60°N, but occur predominantly in  
 202 the midlatitudes and tropics, respectively. An important feature of this cloud classification scheme  
 203 is that the cloud types that can occur in a gridbox vary from month-to-month. In contrast, Scott et  
 204 al. (2020) assign only one cloud type per region for the entire period to define cloud regimes. Since  
 205 clouds vary appreciably over short timescales (Oreopoulous et al., 2016), the identified cloud types  
 206 should be allowed to vary in time to correctly represent TOA flux changes by cloud type.

207 Global statistics (Table 2) of each cloud category for a 20-year climatology  
 208 (07/2002–06/2022) show that Sc has a large local area coverage (52%) and exhibits substantial  
 209 variability, with a monthly SW TOA flux anomaly standard deviation of 4 Wm<sup>-2</sup>. However, the  
 210 Sc cloud class accounts for only 7% of the globe, which reduces its global impact. Local cloud  
 211 fractions for the low cloud types decrease from 52% (Sc) to 20% (Cu), while SSTs increase from  
 212 281 K (Sc) to 300 K (Cu). These general characteristics are consistent with expectation for these  
 213 cloud types (Wood, 2012). Middle clouds have the smallest local fraction (13%) and weakest  
 214 anomaly standard deviations compared to the other cloud types, while polar clouds have largest  
 215 local fraction and average SW flux, but the lowest LW flux and SST.

### 216 **2.3. All-Sky TOA Flux Decomposition**

217 The monthly mean all-sky TOA flux over a latitude range ( $\lambda_1, \lambda_2$ ) and longitude range ( $\phi_1,$   
 218  $\phi_2$ ) can be expressed in terms of its clear and cloudy column contributions from 1°x1° regions as  
 219 follows:

$$220 \quad \bar{F}_{all} = \bar{F}_{clr}^{con} + \sum_{j=1}^n \bar{F}_j^{con} \quad (1)$$

221 where  $\bar{F}_{clr}^{con}$  is the monthly mean clear-sky column flux contribution and  $\bar{F}_j^{con}$  is the monthly mean  
 222 cloud column contribution for cloud class  $j$ , and  $n$  is the number of cloud classes. These are  
 223 calculated as follows:

224 
$$\bar{F}_{clr}^{con} = \frac{1}{W} \int_{\lambda_1}^{\lambda_2} \int_{\phi_1}^{\phi_2} (1 - f_T(\lambda, \phi)) F_{clr}(\lambda, \phi) w_\lambda d\lambda d\phi \quad (2)$$

225 
$$\bar{F}_j^{con} = \frac{1}{W} \int_{\lambda_1}^{\lambda_2} \int_{\phi_1}^{\phi_2} f_j(\lambda, \phi) F_j(\lambda, \phi) w_\lambda d\lambda d\phi \quad (3)$$

226 where  $f_T$  and  $F_{clr}$  are the monthly gridbox total cloud fraction and mean clear-sky flux,  
 227 respectively, and  $f_j$  and  $F_j$  are the monthly gridbox cloud fraction and mean flux for cloud class  $j$ .  
 228 The total cloud fraction  $f_T$  is equal to the sum of the individual  $f_j$ 's, and the weights  $w_\lambda$  are geodetic  
 229 weights whose sum  $W$  over the domain is given by:

230 
$$W = \int_{\lambda_1}^{\lambda_2} \int_{\phi_1}^{\phi_2} w_\lambda d\lambda d\phi \quad (4)$$

231 This decomposition of all-sky TOA flux represents all-sky TOA flux as the sum of area-  
 232 weighted clear and cloudy column fluxes. Anomalies and trends in these contribution terms are  
 233 impacted by area fraction and within-column radiative property changes, but the sum is  
 234 constrained to add to the corresponding all-sky value. We do not correct for non-cloud changes in  
 235 the cloudy columns, nor do we attempt to remove ERF contributions. We expect that the cloud-  
 236 masking error is smaller than that for CRE since it is confined to the cloudy area only rather than  
 237 a gridbox-wide difference between clear-sky and total-sky non-cloud contributions (Soden et al.,  
 238 2008). We plan to extend the methodology to account for cloud-masking contributions in the  
 239 future.

240 **2.4. Validation of MODIS-Based Cloud Fraction Changes**

241 To evaluate MODIS-based cloud fraction changes, Appendix 1 provides a detailed  
 242 comparison of trends in MODIS cloud fraction by cloud type with those from coincident Cloud-  
 243 Aerosol Lidar and Infrared Pathfinder Satellite Observations (CALIPSO) Cloud-Aerosol Lidar  
 244 with Orthogonal Polarization (CALIOP) and CloudSat Cloud Profiling Radar (CPR) data as  
 245 provided in the CALIPSO-CloudSat-CERES-MODIS (CCCM) ReID1 product (Kato et al., 2010,

246 2011). The analysis in Appendix 1 shows that MODIS and CC cloud fraction trends are remarkably  
247 similar for each cloud type, providing confidence in the MODIS-based results. Additional  
248 comparisons between these and other cloud fraction products are provided in Stubenrauch et al.  
249 (2024, this collection), which focuses more on how well the different products agree in their  
250 regional cloud fraction distributions than on temporal variability.

### 251 **3. Results**

#### 252 **3.1. Global, Zonal and Regional Changes in TOA Radiation During CERES Period**

253 As noted in Loeb et al. (2021a, 2022), the CERES record indicates that EEI has  
254 approximately doubled during the CERES period. During the first decade of CERES observations  
255 (03/2000–02/2010), EEI was  $0.5 \pm 0.2 \text{ Wm}^{-2}$  and increased to  $1.0 \pm 0.2 \text{ Wm}^{-2}$  for the most recent  
256 decade (01/2013–12/2022) considered here (Table 3). This is the result of a  $0.9 \pm 0.3 \text{ Wm}^{-2}$  ( $\approx 0.4\%$ )  
257 increase in ASR that is partially offset by a  $0.4 \pm 0.25 \text{ Wm}^{-2}$  ( $\approx 0.2\%$ ) increase in outgoing longwave  
258 radiation (OLR). The corresponding change in incoming solar irradiance is negligible ( $0.02 \pm 0.09$   
259  $\text{Wm}^{-2}$ ). There is satellite evidence that the increase in EEI began during the decade prior to the  
260 CERES period based on a reconstruction of the Earth Radiation Budget Experiment (ERBE) record  
261 (Liu et al., 2020) and satellite altimetry and space gravimetry measurements (Marti et al., 2023).

262 Monthly anomalies in global mean TOA radiation show considerable variability  
263 superimposed over longer-term trends (Figs. 2a-b). Standard deviations in monthly anomalies for  
264 03/2000-12/2022 are 0.7, 0.5 and  $0.7 \text{ Wm}^{-2}$  for ASR,  $-\text{OLR}$  and NET, respectively, and the  
265 corresponding trends are  $0.71 \pm 0.19$ ,  $-0.26 \pm 0.19$ , and  $0.45 \pm 0.18 \text{ Wm}^{-2}$  per decade (uncertainties  
266 given as 2.5–97.5% confidence intervals). Monthly anomalies are consistent across CERES  
267 instruments on different platforms to  $< 0.2 \text{ Wm}^{-2}$  (Loeb et al., 2018) and trends between Terra and  
268 Aqua, the two longest operating missions flying CERES instruments, agree to  $< 0.1 \text{ Wm}^{-2}$  per

269 decade (Loeb et al., 2022). Extensive validation of CERES instrument performance using a range  
270 of consistency tests involving different vicarious Earth targets and regular scans of the Moon  
271 provides further evidence that the CERES instruments are radiometrically stable (Shankar et al.,  
272 2023). The trends from CERES observations also agree with independently estimated trends from  
273 0-2000 m ocean in-situ data to  $< 0.1 \text{ Wm}^{-2}$  per decade (Loeb et al., 2021a, 2022).

274 Analysis of atmospheric climate model simulations with a hierarchy of experiments with  
275 the GFDL CM4/AM4 suggest that the large positive ASR trend is due to additive contributions  
276 from ERF and climate feedback (radiative response) and the weaker negative trend in outgoing  
277 longwave radiation results from compensation between positive ERF and negative climate  
278 feedback contributions (Raghuraman et al., 2021; Hodnebrog et al., 2024). Since the ERF  
279 contributions add together and the climate feedback contributions offset one another, the model  
280 results suggest that ERF is the main driver of the positive trend in NET. However, the magnitudes  
281 of global TOA radiation trends in the climate model simulations are weaker than those in CERES,  
282 and there are large discrepancies in regional trend patterns. Furthermore, coupled climate models  
283 fail to represent observed SST patterns and associated feedbacks (Andrews et al., 2022; Kang et  
284 al., 2023; Olonscheck and Rugenstein, 2024), adding to existing questions about the realism of  
285 climate model changes during the 21<sup>st</sup> Century (Trenberth and Fasullo, 2009). These, together with  
286 substantial updates to SST and forcing datasets, provide additional motivation for further model-  
287 observation comparisons (Schmidt et al., 2023).

288 Zonal average trends for approximately equal-area latitude zones are positive for ASR and  
289 NET in the tropics, sub-tropics, and mid-high latitudes of both hemispheres, while -OLR only  
290 shows appreciable negative trends in the NH subtropics and NH mid-high latitudes (Fig. 3a-c).  
291 Northern and southern hemisphere trends in NET are consistent to  $0.06 \text{ Wm}^{-2}$  per decade due to a

292 compensation between weak ASR and  $-OLR$  hemispheric trend differences of opposite sign  
293 (Table 4). Datsiris and Stevens (2021) also found hemispheric symmetry in reflected SW trends  
294 using CERES data for 03/2000-02/2020. Interestingly, GFDL AMIP climate model simulations  
295 fall within  $0.2 \text{ Wm}^{-2}$  per decade of CERES NH trends for ASR,  $-OLR$  and NET, but underestimate  
296 the ASR trend in the SH by  $\sim 0.5 \text{ Wm}^{-2}$  per decade due to erroneous trends in Antarctic sea ice and  
297 Southern Ocean cloud fraction, resulting in a much larger ASR hemispheric contrast (Raghuraman  
298 et al., 2021).

299         Regionally, significant positive trends in CERES ASR occur off both coasts of North  
300 America, the Seas of Japan and Okhotsk, over the Arctic Ocean between the Kara and East Siberian  
301 Seas, the Southern Ocean to the east of South America, and Antarctica between  $60^{\circ}$ – $120^{\circ}$ E (Fig.  
302 4a). Large positive trends also occur over the equatorial Pacific Ocean, but because interannual  
303 variability is so large in this region due to the El Niño-Southern Oscillation (ENSO), the trends do  
304 not exceed the 2.5-97.5% confidence interval. Negative trends of  $-OLR$ , corresponding to  
305 increased thermal infrared emission to space, are appreciable over the NH eastern Pacific Ocean  
306 and over much of the Arctic (Fig. 4b). These regions are also associated with strong warming (Fig.  
307 4d). Regional net radiation trends are positive over the NH Pacific, Indian and West Atlantic  
308 Oceans, but are mainly negative over the marine stratocumulus region off the west coast of South  
309 America (Fig. 4c). The similarity between the ASR and SST trend patterns is striking (Figs. 4a and  
310 d), particularly over the North Pacific, off the east coast of North America and west coast of South  
311 America.

312         Time series of global mean anomalies in SST, ASR, and  $-OLR$  also share similar features  
313 (Figs. 5a-b). In each case, twelve-month running average anomalies are relatively constant prior  
314 to 2010, and then increase sharply (decrease for  $-OLR$ ) until a maximum is reached during the



315 2015–2016 El Niño event. The anomalies stay relatively flat after this event, albeit with  
316 considerable interannual variability. By comparison, the coherence at interannual timescales  
317 between anomalies in SST and NET radiation is much weaker (Fig. 5c) due to compensation  
318 between ASR and –OLR changes, but both do show a marked increase for the entire period.

319 Coupled climate models show a long-term trend in EEI and SST with anthropogenic  
320 forcing (Collins et al., 2013; Forster et al., 2021). Results in Fig. 5 confirm that increases in EEI  
321 and SST also occur in observations over a 20-year period despite substantial internal variability  
322 from heat exchange between the ocean mixed layer—which directly impacts SST—and the ocean  
323 layers below. Vertical ocean mixing has been shown to add considerable scatter between TOA  
324 radiation and SST trends at decadal timescales (Palmer et al., 2011).

### 325 **3.2 Changes During the Hiatus, Transition-to-El Niño, and Post-El Niño Sub-Periods**

326 We examine the temporal evolution in SST and TOA radiation for the 3 sub-periods, which  
327 we define as follows: (i) “hiatus” (03/2000–05/2010), characterized by a negligible change in the  
328 Multivariate ENSO Index (MEI; Wolter and Timlin, 1998) (Fig. 6a-d), a slower rate of global  
329 warming compared to the longer-term trend (Lewandowsky et al., 2015; Meehl et al., 2013;  
330 Trenberth, 2015a) and to simulations from coupled climate models (Kosaka and Xie, 2013); (ii)  
331 “transition-to-El Niño” (06/2010-05/2016), corresponding to the transition between the 2010-2012  
332 La Niña and 2014-2016 El Niño events; and (iii) “post-El Niño” (06/2016–12/2022),  
333 corresponding to the transition between the 2014–2016 El Niño and the unusual extended 2020-  
334 2022 La Niña (so-called “triple-dip La Niña). During the “transition to El Niño” period, MEI and  
335 SST both show rapid increases that exceed the 2.5-97.5% CI (Figs. 6b and 6d). The SST trend  
336 during this period is  $0.52 \text{ K decade}^{-1}$ , which exceeds the increase during the “hiatus” period by a

337 factor of 5. For the entire period between 03/2000–12/2022, the SST trend is  $0.14 \pm 0.06 \text{ K decade}^{-1}$   
338 and the trend in MEI is near zero.

339 Trends in solar irradiance (SOL) and all-sky reflected SW ( $-SW$ , positive downwards),  
340 ASR,  $-OLR$ , and net radiation (NET) for the three sub-periods and entire time range (Fig. 7a)  
341 reveal that despite marked differences among sub-period trends for ASR,  $-SW$  and  $-OLR$ ,  
342 reaching  $1.3 \text{ Wm}^{-2}$  per decade, NET trends remain within  $0.1 \text{ Wm}^{-2}$  per decade of one another and  
343 the trend over the entire period ( $0.45 \text{ Wm}^{-2}$  per decade). During the “hiatus” the  $-OLR$  trend is  
344 near zero, so that the NET trend is determined by the difference between SOL and  $-SW$ . In  
345 contrast, all-sky  $-SW$  and  $-OLR$  both exceed  $1 \text{ Wm}^{-2}$  per decade in magnitude during the  
346 “transition-to-El Niño” period, but their sum ( $0.26 \text{ Wm}^{-2}$  per decade) and the SOL contribution  
347 ( $0.19 \text{ Wm}^{-2}$  per decade) add to  $\approx 0.45 \text{ Wm}^{-2}$  per decade for NET. This period is characterized by  
348 a substantial warming, leading to greater thermal emission to space from cloud-free areas (Fig.  
349 7b). There is also a decrease in cloud fraction (not shown) that causes a strong ASR contribution  
350 by clouds (Fig. 7c), which compensates for the increased thermal emission. The trend in  $-OLR$   
351 during the “post-El Niño” period is small, and SOL and  $-SW$  contribute approximately equally to  
352 the NET trend. In contrast to the all-sky case, clear-sky NET trends differ by up to  $\sim 1 \text{ Wm}^{-2}$   
353 between sub-periods (Fig. 7b). Changes in clouds compensate for these differences under all-sky  
354 conditions, leading to a very similar all-sky NET trend in each sub-period.

355 It is unclear if the remarkable consistency amongst all-sky NET trends for the sub-periods  
356 occurs by chance or is a robust property of Earth’s energy budget. At shorter time scales than those  
357 defining these sub-periods, there is substantial interannual variability in NET radiation, as shown  
358 in Fig. 2b. Unfortunately, the CERES observational record is too short to test how robust these  
359 results are. Nevertheless, it implies a steady acceleration of climate warming since 2000.

360 It is noteworthy that NET CRE for the full period is near zero (Fig. 7c). Raghuraman et al.  
361 (2023) also show a negligible trend in what they describe as the “cloud feedback component of  
362 CRE”, which is obtained from the difference between CRE and the sum of ERF and cloud masking  
363 contributions. The implication is that net cloud feedback is not statistically significant during the  
364 CERES period. However, this conclusion assumes the model-derived ERF contribution to CRE is  
365 correct. The shortwave ERF contributions are primarily due to greenhouse gas adjustments and  
366 the aerosol-cloud indirect effects, both highly uncertain quantities (Smith et al., 2020).  
367 Furthermore, in Raghuraman et al. (2023) the model shortwave ERF contribution to CRE exceeds  
368 the longwave ERF contribution and accounts for as much as 57% of the total CERES SW CRE.  
369 In their observation-based PRP analysis Loeb et al. (2021a) found a significant positive trend in  
370 the cloud contribution to NET all-sky TOA flux, but aerosol-cloud indirect effects and greenhouse  
371 gas adjustments and were not removed from the cloud contribution. The uncertainty surrounding  
372 ERF thus makes it challenging to unambiguously isolate the net effect of clouds during the CERES  
373 period.

### 374 **3.3 TOA Radiation Changes by Cloud Type**

375 The cloud classes (Section 2.2) and all-sky TOA flux decomposition (Section 2.3) provide  
376 a framework to assess TOA radiation changes by cloud type using FBCT. Since the CERES FBCT  
377 product uses data from both Terra and Aqua, the time period considered is limited to  
378 07/2002–12/2022. Given that EBAF TOA global trends for this period are very similar to those  
379 for the full CERES period (Table 5), we expect results for the shorter period to be representative  
380 of the full period. We also find good agreement between EBAF and FBCT all-sky, clear-sky, and  
381 CRE trends for 07/2002–12/2022 (Table 5). The reason for the larger clear-sky –OLR difference

382 is unknown. One contributing factor could be because of cloud mask differences as FBCT is a  
383 daytime-only product while EBAF uses both daytime and nighttime observations.

384 To illustrate the utility of the all-sky TOA flux decomposition framework, we compare  
385 global trends in TOA fluxes for all-sky, clear-sky and CRE alongside cloud fraction-weighted  
386 contributions computed using Eqs. (1-4) in Fig. 8. While the trend in net CRE is weak due to  
387 compensation between  $-SW$  and  $-OLR$  components, the trend for the area-weighted cloudy  
388 contribution is appreciable due to a large positive trend in  $-SW$  and negligible  $-OLR$  trend.  
389 Without any cloud-masking adjustments in the cloudy regions, this result is already comparable to  
390 what is obtained using PRP analysis (see Fig 2 in Loeb et al., 2021a). We expect that after  
391 subtracting cloud-masking contributions, agreement with the PRP result will improve. After the  
392 corrections are made, trends in the  $-SW$ ,  $-OLR$  and NET area-weighted cloudy contribution  
393 should decrease because part of the positive  $-SW$  trend is impacted by decreases in surface albedo  
394 from declining sea-ice coverage during the CERES period, and part of the  $-OLR$  trend is  
395 associated with reduced emission resulting from increases in water vapor and WMGG above the  
396 cloud top (Raghuraman et al., 2023). Results in Fig. 8 show that the all-sky decomposition  
397 approach in Section 2.3 provides a better framework than CRE for assessing the radiative impacts  
398 of cloud changes. The key difference with the CRE approach is that the all-sky decomposition  
399 separates changes from clear and cloudy areas whereas the CRE approach can only provide reliable  
400 results if there are no changes in cloud-free conditions, which is unrealistic.

401 TOA radiation and cloud fraction changes by cloud type for different latitude zones (Figs.  
402 9-12) provide context for the hemispheric and global trends (Table 4). Since the contribution from  
403 each cloud class is an area fraction-weighted quantity over each latitude zone, the sum of all  
404 contributions plus the clear-sky contribution is equal to the total all-sky value. Decreases in low

405 and middle cloud fraction and reflection between 20°-60°N (Figs. 9b-c, 10b-c) and reduced  
406 reflection from cloud-free areas between 42°-90°N (Fig. 9a) are the primary reasons for the NH  
407 ASR increase of  $0.8 \text{ Wm}^{-2} \text{ decade}^{-1}$  in Table 4. Low cloud changes are primarily from Sc between  
408 20°-42°N, while Sc, SCT and Cu all contribute to the low cloud ASR increase between 42°-60°N  
409 (Fig. 11). Regionally, these changes occur over the eastern and northern Pacific and off the east  
410 coast of North America, and coincide with large increases in SST (Fig. 4d). Other studies have  
411 noted the significant low cloud response to SST in these regions (Myers et al., 2018; Andersen et  
412 al., 2023).

413         Interestingly, while there is a marked increase in clear-sky fraction in the NH subtropics  
414 between 20°-42°N (Fig. 10a), the corresponding ASR trend contribution is near zero (Fig. 9a).  
415 This is likely because of a decrease in aerosol optical depth in this latitude range during the CERES  
416 period (Zhao et al., 2017; Paulot et al., 2018; Loeb et al., 2021b), which compensates for the  
417 increased clear-sky frequency, resulting in a near-zero ASR trend contribution. While high clouds  
418 contribute little to the overall NH ASR trend, there is a notable increase in high cloud fraction  
419 between 42° and 60°N (Fig. 10d) that causes a negative ASR trend (Fig. 9d). Increased thermal  
420 emission in cloud-free conditions combined with high cloud changes contribute most to the  $-0.33$   
421  $\text{Wm}^{-2} \text{ decade}^{-1}$  NH  $-\text{OLR}$  change in Table 4. The increase in SST between 20° and 42°N likely  
422 contributes to a sharp increase in clear-sky thermal infrared emission ( $-\text{LW}$  trend of  $-1.6 \text{ Wm}^{-2}$   
423 per decade) (Fig. 12a) while the increase in high cloud thermal emission between 42° and 60°N is  
424 associated with increased cloud fraction (Fig. 12d).

425         The ASR trend of  $0.62 \text{ Wm}^{-2} \text{ decade}^{-1}$  in the SH (Table 4) is primarily associated with  
426 decreases in middle cloud reflection (Fig. 9c) and a weaker reduction in low cloud reflection (Fig.  
427 9b). Middle cloud fractions decrease by almost the same amount in each SH latitude zone (Fig.

428 10c) while high cloud fraction increases between 42° and 60°S (Figs. 10d), resulting in a weak  
429 negative ASR trend contribution to ASR (Figs. 9d). In contrast to the NH, -LW cloud trends in  
430 the SH are weak and largely cancel one another.

#### 431 **4. Discussion**

432 A key limitation of relying solely on observations to explain TOA radiation changes is that  
433 some of the underlying processes involved are difficult to isolate. For example, there is evidence  
434 that anthropogenic aerosol effective radiative forcing is weakening due to a decline in  
435 anthropogenic primary aerosol and aerosol precursor emissions (Quaas et al., 2022). Observations  
436 can provide estimates of the influence of aerosol-radiation interactions (Bellouin et al., 2005;  
437 Subba et al., 2020; Loeb et al., 2021b; Szopa et al., 2021), but the much stronger forcing  
438 contribution from aerosol-cloud interactions is more difficult to quantify as both clouds and  
439 aerosols are impacted by their environment (e.g., meteorology) in addition to having a two-way  
440 interaction between them (Gryspeerdt et al., 2016; McCoy et al., 2020). Furthermore, passive  
441 satellite aerosol retrievals are more uncertain in cloudy regions, and cloud retrievals are more  
442 uncertain in environments with abundant aerosol (Koren et al., 2007; Loeb and Schuster, 2008;  
443 Gryspeerdt et al., 2016). This makes it challenging to unambiguously quantify how aerosol and  
444 cloud changes separately influence trends in ASR, which we show track closely with trends in  
445 SST, particularly over stratocumulus regions off the west coast of North America and over the  
446 North Pacific Ocean (see also Andersen et al., 2022; Myers et al., 2018). Establishing causality  
447 between observed SST and ASR changes also has its challenges as these share a two-way  
448 interaction (Trenberth et al., 2015b).

449 Nevertheless, progress is being made on the use of satellite observations for studying  
450 aerosols. A recent study by Wall et al. (2022) introduces a new method that removes confounding

451 meteorological factors from observed sulfate–low-cloud relationships and narrows the uncertainty  
452 in aerosol forcing. Studies by Yuan et al. (2022) and Diamond (2023) use satellite observations to  
453 quantify the impact of sulfur regulations for shipping fuel on aerosol indirect forcing. Both studies  
454 find evidence for reduced radiative cooling by clouds following new regulations limiting sulfur  
455 emissions from the shipping industry by the International Maritime Organization 2020.

456 A longer TOA ERB observational record and new model output from CERESMIP provides  
457 new opportunities to determine how best to use observations and models for improving our  
458 understanding of the underlying process related to EEI changes. Current climate model simulations  
459 show similar patterns in regional TOA flux changes as observations, but the magnitudes of the  
460 changes differ markedly (Loeb et al., 2020), particularly over cloudy extratropical regions  
461 (Trenberth and Fasullo, 2010; Zelinka et al., 2020). Similarly, the EEI trends from Raghuraman et  
462 al. (2021) are systematically lower compared to CERES. Conversely, if we find agreement  
463 between trends in TOA radiation in observations and climate model simulations, do they agree for  
464 the right reasons? To answer this, it will be necessary to use additional datasets and climate model  
465 output describing cloud and aerosol changes. Our comparisons with CC (Appendix 1) provide  
466 some confidence that the imager-based cloud changes are realistic. This means that there is some  
467 hope that meaningful comparisons between observed and model cloud changes is within reach.

## 468 **5. Summary and Conclusions**

469 CERES observations show that Earth’s energy imbalance (EEI) has doubled from  $0.5\pm 0.2$   
470  $\text{Wm}^{-2}$  during the first 10 years of this century to  $1.0\pm 0.2 \text{ Wm}^{-2}$  during the past decade. This has  
471 led to accelerated increases in global mean temperature, sea level rise, ocean heating, and snow  
472 and sea ice melt. The increase in EEI is the result of a  $0.9\pm 0.3 \text{ Wm}^{-2}$  increase absorbed solar  
473 radiation (ASR) that is partially offset by a  $0.4\pm 0.25 \text{ Wm}^{-2}$  increase in outgoing longwave

474 radiation (OLR). Since most of the energy added to the climate system associated with EEI ends  
475 up as heat storage in the ocean, changes in TOA radiation and ocean heat uptake (OHU) derived  
476 from in situ ocean data should track one another. Indeed, recently published analyses indicate that  
477 when in situ ocean measurements are supplemented with other data to fill in sparsely sampled  
478 regions, there is good agreement between variations and trends in OHU and CERES EEI for the  
479 Argo period between 2005 and 2019 (Loeb et al., 2021a; Hakuba et al. 2024, this collection).

480 Regional patterns of CERES ASR,  $-OLR$  and SST trends are similar, particularly over the  
481 North Pacific, off the east coast of North America and west coast of South America. Time series  
482 of global mean anomalies in SST, ASR, and  $-OLR$  also share similar features. In each case,  
483 twelve-month running average anomalies are relatively constant prior to 2010 (“hiatus” period),  
484 increase markedly (decrease for  $-OLR$ ) prior to the 2015-2016 El Niño event (“transition-to-El  
485 Niño” period), and remain relatively flat after this event (“post-El Niño” period). Despite marked  
486 differences in global ASR and global  $-OLR$  trends between these sub-periods, NET trends remain  
487 strikingly within  $0.1 \text{ Wm}^{-2}$  per decade of one another. Since climate stabilization requires the  
488 climate forcing or net radiative imbalance to restore to zero, an increase in Earth’s radiative energy  
489 imbalance implies an acceleration of climate change rather than a continued, steady heating  
490 implied by a constant imbalance (e.g. von Shuckman et al., 2023). However, we note that NET  
491 radiation exhibits appreciable internal variability at interannual time scales. A longer observational  
492 record is needed to determine how robust these findings are.

493 We compare global trends in TOA fluxes of CRE alongside an alternate approach that uses  
494 the CERES FluxbyCldTyp (FBCT) product to isolate the cloudy and clear-sky contributions to all-  
495 sky TOA flux trends. While the trend in net CRE is weak due to compensation between  $-SW$  and  
496  $-OLR$  components, the trend for the cloudy sky contribution is appreciable due to a large positive



497 trend in  $-SW$  (i.e., reduced cloud reflection) and negligible  $-OLR$  trend. The latter is comparable  
498 to what is obtained using the PRP method and thus provides a better framework than CRE for  
499 assessing the radiative impacts of cloud changes. Further refinement would be required to account  
500 for cloud-masking contributions in cloudy areas. Isolating the cloud contribution also requires  
501 removing the contribution from effective radiative forcing (aerosol-cloud indirect effects and  
502 greenhouse gas adjustments), which is highly uncertain.

503         When the cloudy sky contribution is stratified by cloud type, we find that decreases in low  
504 and middle cloud fraction and reflection and reduced reflection from cloud-free areas in mid-high  
505 latitudes are the primary reasons for increasing ASR trends in the NH. Low cloud changes are  
506 primarily from Sc between  $20^\circ$  and  $42^\circ N$ , while Sc, SCT and Cu all contribute to the low cloud  
507 ASR increase between  $42^\circ$  and  $60^\circ N$ . In the SH the increase in ASR is primarily from decreases  
508 in middle cloud reflection and a weaker reduction in low cloud reflection. Increased thermal  
509 emission in cloud-free conditions combined with high cloud changes contribute most to the  
510 increase in OLR.

511         Climate model AMIP simulations suggest that the larger ASR increase observed during the  
512 CERES period is due to additive contributions from effective radiative forcing (ERF) and climate  
513 response to warming and its spatial pattern, while the weaker OLR change is associated with  
514 compensation between increasing ERF from continued emission of well-mixed greenhouse gases  
515 and increased infrared cooling to space relating to the radiative response to warming (Raghuraman  
516 et al., 2021; Hodnebrog et al., 2024). Model-based attribution of the CERES results are limited in  
517 number because the CMIP6 protocol ends in 2014. The new Atmospheric Model Intercomparison  
518 Project (AMIP) simulations proposed as part of CERESMIP (Schmidt et al., 2023) will provide

519 updated model simulations through 2021 and will use input data sets, greatly expanding  
520 opportunitites to assess model performance and attribution of the observed EEI trend.

521  
522

523 **Acknowledgments** We thank the CERES science, algorithm and data management teams and  
524 the NASA Science Mission Directorate for supporting this research. This is PMEL contribution  
525 number 5554 and CIMAR contribution number 23-404. RPA was funded by funded by the  
526 National Centre for Earth Observation Grant Number: NE/RO16518/1. CERES data were  
527 obtained from [http://ceres.larc.nasa.gov/compare\\_products.php](http://ceres.larc.nasa.gov/compare_products.php). ERA5 data are publicly  
528 available via the Copernicus Climate Change Service climate ([https://confluence.ecmwf.  
529 int/display/CKB/](https://confluence.ecmwf.int/display/CKB/)). This paper is an outcome of the Workshop "Challenges in Understanding the  
530 Global Water Energy Cycle and its Changes in Response to Greenhouse Gas Emissions" held at  
531 the International Space Science Institute (ISSI) in Bern, Switzerland (26–30 September 2022).

## 532 **Appendix 1: Cloud Fraction Trend Comparison Between MODIS and CC**

533 We compare MODIS-based cloud fraction trends with those from CALIPSO and CloudSat  
534 provided in the CCCM ReID1 product (Kato et al., 2010, 2011). The period considered is 01/2008-  
535 12/2017. As CALIPSO and/or CloudSat measurements are unavailable  $\approx 20\%$  of the time after  
536 2011, we only include months in which all three instruments provide valid measurements. To  
537 ensure consistent spatial sampling, we only use MODIS cloud properties from CERES footprints  
538 that are collocated with the CALIPSO and Cloudsat (CC) satellite tracks. MODIS cloud fraction  
539 is determined for each MODIS pixel using the CERES cloud algorithm (Minnis et al., 2021). The  
540 CALIPSO cloud mask is from CALIPSO Vertical Feature Mask (VFM) version 4 product  
541 (Vaughan et al. 2009) with a threshold of the cloud aerosol discrimination (CAD) score  $\geq 20$  and  
542 a horizontal averaging scale for cloud detection  $\leq 20$  km. Since CALIPSO detects optically thin  
543 ice clouds that are often missed by MODIS, we exclude optically thin ice clouds using the  
544 following criterion: if the cumulative cloud optical depth ( $\tau$ ) from the top is smaller than 0.3, the  
545 CALIPSO cloud layer is removed and treated as clear. For consistency, a  $\tau$  filtering ( $\tau \geq 0.3$ ) is  
546 also applied to MODIS. We find that the MODIS cloud trends with and without the  $\tau$  filtering are  
547 nearly identical (not shown), meaning that the occurrence of  $\tau < 0.3$  is small. The CloudSat cloud  
548 mask is from the CloudSat 2B-GEORPOF release 5 (R05) product (Sassen and Wang 2008) with  
549 a threshold of the cloud mask value  $\geq 30$  and the radar reflectivity  $> -25$  dBZ. The radar reflectivity  
550 condition is considered to minimize the impact of the degradation of the CloudSat Cloud Profiling  
551 Radar (CPR) sensor (Mathew Lebsock, personal communication). To combine CC cloud layers  
552 we choose the closest CloudSat pixel for a given CALIPSO pixel.

553 After merging CALIPSO and CloudSat cloud layers, the cloud top height of the uppermost  
554 layer is used to assign the cloud type. This is because MODIS usually detects the uppermost cloud

555 layers in the case of multi-layered clouds. The CC cloud top height is converted into the cloud top  
556 pressure using pressure profiles of the Global Modeling and Assimilation Office (GMAO)'s  
557 Goddard Earth Observing System Data Assimilation System (GEOS-DAS V5.4.1) product  
558 (Rienecker et al., 2008).

559 To evaluate MODIS cloud fraction trends, we compare coincident MODIS and CC during  
560 the common period from 01/2008 to 12/2017 for the same cloud types (Figs. 13a-d). Since this  
561 comparison is for a much shorter period, these results need not match those in Fig. 10. Furthermore,  
562 because ~20% of the CC data after 2011 are missing, the trends may not even be representative  
563 of 2008–2018. Rather, the intent is to provide an independent assessment of the MODIS results  
564 using CC.

565 Cloud changes inferred from CC are sensitive to the cloud selection criteria applied in the  
566 analysis. For example, if we include CALIPSO clouds with small cloud optical depth values ( $<$   
567 0.3), high cloud trends become increasingly negative (not shown). In addition, the horizontal  
568 averaging scale for CALIPSO cloud detection also impacts the results. If CALIPSO water clouds  
569 with cloud-top  $<$  4 km are detected from a single lidar beam (1/3 km resolution) without horizontal  
570 averaging, decadal trends of low clouds are reduced relative to that where horizontal averaging is  
571 included. We estimate uncertainties in CC cloud fraction trends by combining three factors. The  
572 first factor is related to the uncertainty of the linear regression as standard errors ( $= \sigma_A$ ). The second  
573 factor is related to the uncertainty related to the  $\tau$  filtering ( $= \sigma_B$ ). We estimate  $\sigma_B$  as the difference  
574 in the decadal trends with and without the  $\tau$  filtering. The third factor is related to the uncertainty  
575 related to the horizontal averaging scales of CALIPSO water clouds below 4 km ( $= \sigma_C$ ). We  
576 estimate the value of  $\sigma_C$  as the difference in the decadal trends with 1/3 km scales of clouds and  
577 with 1/3, 1, 5, and 20 km averaging scales of water clouds below 4 km. The overall uncertainty is

578 determined by summing the individual contributions in quadrature ( $=(\sigma_A^2 + \sigma_B^2 + \sigma_C^2)^{1/2}$ ). These  
579 are given as error bars in CC cloud trends.

580         MODIS and CC show remarkably consistent cloud fraction trends for each cloud type in  
581 the SH (Figs. 13c-d). Both show a large negative trend in Sc and a large positive trend in SCT, and  
582 weaker Cu, Mid, High and Polar cloud trends. The large error bar for CC high clouds is due to a  
583 greater sensitivity to our approach used to filter out thin clouds with optical depths  $< 0.3$  that are  
584 below the MODIS detection threshold (Section 2.1). Differences are larger for the clear-sky  
585 fraction trend with MODIS showing no trend and CC showing a decrease in clear-sky fraction.  
586 With the exception of the Polar cloud case, the NH MODIS and CC cloud trends are generally  
587 weaker than those in the SH and show less agreement. Both show a significant decrease in Sc, but  
588 the magnitude of the decrease is larger for MODIS. There is a large discrepancy in clear-sky  
589 fraction, with MODIS showing an increase and CC showing little change. At global scale, the main  
590 features that stand out are the SC and SCT trends, which MODIS and CC capture. These  
591 comparisons suggest that MODIS is capable of capturing large changes in cloud fraction, but  
592 weaker trends are more uncertain.  
593

## References

- 594  
595  
596 Andersen, H., J. Cermak, , L. Zipfel, and T. A. Myers, 2022: Attribution of observed recent  
597 decrease in low clouds over the northeastern Pacific to cloudcontrolling factors. *Geophys.*  
598 *Res. Lett.*, 49, e2021GL096498. <https://doi.org/10.1029/2021GL096498>.
- 599 Andrews, T., A. Bodas-Salcedo, J. M. Gregory, Y. Dong, K. C. Armour, D. Paynter, D., et al.,  
600 2022: On the effect of historical SST patterns on radiative feedback. *J. Geophys. Res.*, 127,  
601 e2022JD036675. <https://doi.org/10.1029/2022JD036675>
- 602 Bellouin, N., O. Boucher, J. Haywood, and M. S. Reddy, 2005: Global estimate of aerosol direct  
603 radiative forcing from satellite measurements, *Nature*, 438, 1138–1141,  
604 <https://doi.org/10.1038/nature04348>.
- 605 Cheng, L. J., and Coauthors, 2024: New record ocean temperatures and related climate indicators  
606 in 2023. *Adv. Atmos. Sci.*, <https://doi.org/10.1007/s00376-024-3378-5>.
- 607 Cole, J., H. W. Barker, N. G. Loeb, and K. von Salzen, 2011: Assessing simulated clouds and  
608 radiative fluxes using properties of clouds whose tops are exposed to space. *J. Climate*, 24,  
609 2715-2727. doi: 10.1175/2011JCLI3652.1
- 610 Collins, M., and co-authors, 2013: Long-term Climate Change: Projections, Commitments and  
611 Irreversibility. In: *Climate Change 2013: The Physical Science Basis. Contribution of*  
612 *Working Group I to the Fifth Assessment Report of the Intergovernmental Panel on Climate*  
613 *Change* [Stocker, T.F., D. Qin, G.-K. Plattner, M. Tignor, S.K. Allen, J. Boschung, A.  
614 Nauels, Y. Xia, V. Bex and P.M. Midgley (eds.)]. Cambridge University Press, Cambridge,  
615 United Kingdom and New York, NY, USA.

616 Datseris, G., and B. Stevens, 2021: Earth's albedo and its symmetry. AGU Advances, 2,  
617 e2021AV000440, <https://doi.org/10.1029/2021AV000440>.

618 Diamond, M. S., 2023: Detection of large-scale cloud microphysical changes within a major  
619 shipping corridor after implementation of the International Maritime Organization 2020 fuel  
620 sulfur regulations. Atmos. Chem. Phys., 23, 8259-8269. [https://doi.org/10.5194/acp-23-](https://doi.org/10.5194/acp-23-8259-2023)  
621 8259-2023

622 Doelling, D. R., N. G. Loeb, D. F. Keyes, M. L. Nordeen, D. Morstad, C. Nguyen, B. A.  
623 Wielicki, D. F. Young, M. Sun, 2013: Geostationary Enhanced Temporal Interpolation for  
624 CERES Flux Products, *Journal of Atmospheric and Oceanic Technology*, **30**(6), 1072-1090.  
625 doi: [10.1175/JTECH-D-12-00136.1](https://doi.org/10.1175/JTECH-D-12-00136.1)

626 Eitzen, Z. A., W. Su, K.-M. Xu, N. Loeb, M. Sun, D. Doelling, ... A. Bodas-Salcedo, 2017:  
627 Evaluation of a general circulation model by the CERES flux-by-cloud type simulator. J.  
628 Geophys. Res. Atmos., 122, 10,655–10,668. <https://doi.org/10.1002/2017JD027076>

629 Eyring, V., S. Bony, G. A. Meehl, C. A., Senior, B. Stevens, R. J. Stouffer, and K. E. Taylor,  
630 2016: Overview of the Coupled Model Intercomparison Project Phase 6 (CMIP6)  
631 experimental design and organization, Geosci. Model Dev., 9, 1937–1958,  
632 <https://doi.org/10.5194/gmd-9-1937-2016>, 2016.

633 Forster, P., and co-authors, 2021: The Earth's Energy Budget, Climate Feedbacks, and Climate  
634 Sensitivity. In *Climate Change 2021: The Physical Science Basis. Contribution of Working*  
635 *Group I to the Sixth Assessment Report of the Intergovernmental Panel on Climate Change*  
636 [Masson-Delmotte, V., P. Zhai, A. Pirani, S.L. Connors, C. P.an, S. Berger, N. Caud, Y.  
637 Chen, L. Goldfarb, M.I. Gomis, M. Huang, K. Leitzell, E. Lonnoy, J.B.R. Matthews, T.K.  
638 Maycock, T. Waterfield, O. Yelek.i, R. Yu, and B. Zhou (eds.)]. Cambridge University



639 Press, Cambridge, United Kingdom and New York, NY, USA, pp. 923–1054,  
640 doi:10.1017/9781009157896.009

641 Gryspeerdt, E., J. Quaas, and N. Bellouin, 2016: Constraining the aerosol influence on cloud  
642 fraction, *J. Geophys. Res.*, 121, 3566–3583, doi: 10.1002/2015JD023744.

643 Hakuba, M. Z., T. Frederikse, F. W. Landerer, 2021: Earth's Energy Imbalance From the Ocean  
644 Perspective (2005–2019). *Geophysical Research Letters*, 48(16), e2021GL093624.  
645 doi: [10.1029/2021GL093624](https://doi.org/10.1029/2021GL093624).

646 Hakuba, and Co-Authors, 2024: Trends and Variability in Earth's Energy Imbalance and Ocean  
647 Heat Uptake since 2005, *Surveys in Geophysics* (submitted, this collection).

648 Hansen, J., Nazarenko, L., Ruedy, R., Sato, M., Willis, J., Del Genio, A., Koch, D., Lacis, A.,  
649 Lo, K., Menon, S., Novakov, T., Perlwitz, J., Russell, G., Schmidt, G. A., and Tausnev, N.,  
650 2005: Earth's energy imbalance: Confirmation and implications, *Science*, 308, 1431–1435,  
651 doi:10.1126/science.1110252

652 Held, I. M. et al., 2019: Structure and performance of GFDL's CM4.0 climate model. *J. Adv.*  
653 *Modeling Earth Syst.* 11.11, 3691–3727.

654 Hersbach, H., B. Bill, P. Berrisford, S. Hirahara, A. Horanyi, A., and J. Munoz-Sabater, et al.,  
655 2020: The ERA5 global reanalysis. *Quarterly Journal of Royal Meteorological Society*, 146,  
656 1999–2049. <https://doi.org/10.1002/qj.3803>

657 Hodnebrog, Ø., G. Myhre, C. Jouan, T. Andrews, P. M. Forster, H. Jia, N. G. Loeb, D. J. L.  
658 Olivié, D. Paynter, J. Quaas, S. P. Raghuraman, and M Schulz, 2024: Recent reductions in  
659 aerosol emissions have increased Earth's energy imbalance. *Nature Comm. Earth &*  
660 *Environ.*, <https://doi.org/10.1038/s43247-024-01324-8>.

661 Johnson, G. C., J. M. Lyman, and N. G. Loeb, 2016: Improving estimates of Earth's energy  
662 imbalance. *Nature Climate Change*(7), 639–640. <https://doi.org/10.1038/nclimate3043>

663 Kang, S. M., P. Ceppo, Y. Yu, and I.-S. Kang, 2023: Recent global climate feedback controlled  
664 by Southern Ocean cooling. *Nat. Clim. Change*, 16, 775-780.  
665 <https://doi.org/10.1038/s41561-023-01256-6>

666 Kato, S., S. Sun-Mack, W. F. Miller, F. G. Rose, Y. Chen, P. Minnis, and B. A. Wielicki, 2010:  
667 Relationships among cloud occurrence frequency, overlap, and effective thickness derived  
668 from CALIPSO and CloudSat merged cloud vertical profiles. *J. Geophys. Res.*, 115,  
669 D00H28, <https://doi.org/10.1029/2009JD012277>.

670 Kato, S., and Coauthors, 2011: Improvements of top-of-atmosphere and surface irradiance  
671 computations with CALIPSO-, CloudSat-, and MODIS-derived cloud and aerosol properties.  
672 *J. Geophys. Res.*, 116, D19209, <https://doi.org/10.1029/2011JD016050>.

673 Koren, I., L. A. Remer, Y. J. Kaufman, Y. Rudich, and J. V. Martins, 2007: On the twilight zone  
674 between clouds and aerosols. *Geophys. Res. Lett.*, 34, doi:10.1029/2007GL029253.

675 Kosaka, Y., and S.-P. Xie, 2013: Recent global-warming hiatus tied to equatorial Pacific surface  
676 cooling. *Nature*, 501, 403-407, <https://doi.org/10.1038/nature12534>.

677 Kramer, R. J., He, H., Soden, B. J., Oreopoulos, L., Myhre, G., Forster, P. M., & Smith, C. J.  
678 (2021). Observational evidence of increasing global radiative forcing. *Geophysical Research*  
679 *Letters*, 48, e2020GL091585. <https://doi.org/10.1029/2020GL091585>

680 Lewandowsky, S., J. S. Risbey, and N. Oreskes, 2015: On the definition and identifiability of the  
681 alleged “hiatus” in global warming. *Sci. Rep.* 5, DOI: 10.1038/srep16784.

682 Li, Z., M. H. England, and S. Groeskamp, 2023: Recent acceleration in global ocean heat  
683 accumulation by mode and intermediate waters. *Nature Comm.*, 14:6888,  
684 <https://doi.org/10.1038/s41467-023-42468-z>

685 Liu, C., R. P. Allan, M. Mayer, P. Hyder, D. Desbruyères, L. Cheng, J. Xu, F. Xu, and Y. Zhang,  
686 2020: Variability in the global energy budget and transports 1985–2017. *Clim. Dynam.*, 55,  
687 3381-3396, <https://doi.org/10.1007/s00382-020-05451-8>

688 Loeb, N. G., and G. L. Schuster, 2008: An observational study of the relationship between  
689 cloud, aerosol and meteorology in broken low-level cloud conditions, *J. Geophys.*  
690 *Res.*, **113**, D14214, doi:[10.1029/2007JD009763](https://doi.org/10.1029/2007JD009763).

691 Loeb, N.G., B.A. Wielicki, D.R. Doelling, G.L. Smith, D.F. Keyes, S. Kato, N.M. Smith, and T.  
692 Wong, 2009: Towards optimal closure of the earth's top-of-atmosphere radiation budget. *J.*  
693 *Climate*, **22**, 748-766.

694 Loeb, N. G., D. R. Doelling, H. Wang, W. Su, C. Nguyen, J. G. Corbett, L. Liang, C. Mitrescu,  
695 F. G. Rose, and S. Kato, 2018: Clouds and the Earth's Radiant Energy System (CERES)  
696 Energy Balanced and Filled (EBAF) Top-of-Atmosphere (TOA) Edition 4.0 data product, *J.*  
697 *Climate*, 31, 895-918. doi: 10.1175/JCLI-D-17-0208.1

698 Loeb, N. G., H. Wang, R. P. Allan, T. Andrews, K. Armour, J.N.S. Cole, et al., 2020: New  
699 generation of climate models track recent unprecedented changes in earth's radiation budget  
700 observed by CERES. *Geophys. Res. Lett.*, 47, doi:[10.1029/2019GL086705](https://doi.org/10.1029/2019GL086705)

701 Loeb, N. G., G. C. Johnson, T. J. Thorsen, J. M. Lyman, F. G. Rose, and S. Kato, 2021a:  
702 Satellite and ocean data reveal marked increase in Earth's heating rate. *Geophys. Res. Lett.*,  
703 48, e2021GL093047. <https://doi.org/10.1029/2021GL093047>.

704 Loeb, N. G., W. Su, N. Bellouin, Y. Ming, 2021b: Changes in Clear-Sky Shortwave Aerosol  
705 Direct Radiative Effects Since 2002. *J. Geophys. Res.*, 126(5), e2020JD034090.  
706 doi: <https://doi.org/10.1029/2020JD034090>.

707 Loeb, N. G., M. M. Mayer, S. Kato, J. T. Fasullo, H. Zuo, R. Senan, J. M. Lyman, G. C.  
708 Johnson, and M. Balmaseda, 2022: Evaluating twenty-year trends in Earth's energy flows  
709 from observations and reanalyses. *J. Geophys. Res.*, 127, e2022JD036686,  
710 <https://doi.org/10.1029/2022JD036686>.

711 Loeb, N. G., F. G. Rose, S. Kato, D. A. Rutan, W. Su, H. Wang, D. R. Doelling, W. L. Smith, A.  
712 Gettelman, 2020: Toward a Consistent Definition between Satellite and Model Clear-Sky  
713 Radiative Fluxes. *J. Climate*, 33(1), 61-75. doi: [10.1175/JCLI-D-19-0381.1](https://doi.org/10.1175/JCLI-D-19-0381.1)

714 Marti, F., Rousseau, V., Ablain, M., Fraudeau, R., Meyssignac, B., and Blazquez, A.: Monitoring  
715 the global ocean heat content from space geodetic observations to estimate the Earth energy  
716 imbalance, *State Planet Discuss.* [preprint], <https://doi.org/10.5194/sp-2023-26>, in review,  
717 2023.

718 McCoy, D. T., P. Field, H. Gordon, G. S. Elsaesser, D. P. Grosvenor, 2020: Untangling  
719 causality in midlatitude aerosol-cloud adjustments. *Atmos. Chem. Phys.* 20, 4085–4103.

720 Meehl, G. A., A. Hu, J. M. Arblaster, J. Fasullo, and K. E. Trenberth, 2013: Externally forced  
721 and internally generated decadal climate variability associated with the Interdecadal Pacific  
722 Oscillation. *J. Climate*, 26, 7298-7310. DOI: [10.1175/JCLI-D-12-00548.1](https://doi.org/10.1175/JCLI-D-12-00548.1)

723 Meyssignac, B., et al., 2023: How accurate is accurate enough for measuring sea-level rise and  
724 variability. *Nat. Clim. Change*, 13, 796-804. <https://doi.org/10.1038/s41558-023-01735-z>

725 Minière, A., K. von Schuckmann, J.-B. Sallée, and L. Vogt, 2023: Robust acceleration of Earth  
726 system heating observed over the past six decades. *Sci. Reports*, 13:22975,  
727 <https://doi.org/10.1038/s41598-023-49353-1>

728 Minnis, P., and Coauthors, 2008: Cloud detection in non-polar regions for CERES using TRMM  
729 VIRS and Terra and Aqua MODIS data. *IEEE Trans. Geosci. Remote Sens.*, 46, 3857–3884,  
730 <https://doi.org/10.1109/TGRS.2008.2001351>.

731 Minnis, P., and Coauthors, 2011a: CERES Edition-2 cloud property retrievals using TRMM  
732 VIRS and Terra and Aqua MODIS data—Part I: Algorithms. *IEEE Trans. Geosci. Remote*  
733 *Sens.*, 49, 4374–4400, <https://doi.org/10.1109/TGRS.2011.2144601>.

734 Minnis, P., and Coauthors, 2011b: CERES Edition-2 cloud property retrievals using TRMM  
735 VIRS and Terra and Aqua MODIS data—Part II: Examples of average results and  
736 comparisons with other data. *IEEE Trans. Geosci. Remote Sens.*, 49, 4401–4430,  
737 <https://doi.org/10.1109/TGRS.2011.2144602>.

738 Myers, T. A., C. R. Mechoso, G. V. Cesana, M. J. DeFlorio, and D. E. Waliser, 2018: Cloud  
739 feedback key to marine heatwave off Baja California. *Geophys. Res. Lett.*, 45(9), 4345–  
740 4352. <https://doi.org/10.1029/2018GL078242>.

741 Minnis, P., and Coauthors, 2021: CERES MODIS cloud product retrievals for edition 4—Part I:  
742 Algorithm changes. *IEEE Trans. Geosci. Remote Sens.*, 59, 2744–2780,  
743 <https://doi.org/10.1109/TGRS.2020.3008866>

744 Myers, T., and J. R. Norris, 2015: On the relationship between subtropical clouds and  
745 meteorology in observations and CMIP3 and CMIP5 models. *J. Climate*, 28, 2945-2967.  
746 DOI: 10.1175/JCLI-D-14-00475.1

747 Myers, T., M.D. Zelinka, and S.A. Klein, 2023: Observational constraints on the cloud feedback  
748 pattern effect. *J. Climate*, 36, 6533-6545. <https://doi.org/10.1175/JCLI-D-22-0862.1>

749 Olonscheck, D., and M. Rugenstein, 2024: Coupled climate models systematically underestimate  
750 radiation response to surface warming. *Geophysical Research Letters*, 51, e2023GL106909.  
751 <https://doi.org/10.1029/2023GL106909>.

752 Oreopoulos, L., N. Cho, D. Lee, S. Kato, 2016: Radiative effects of global MODIS cloud  
753 regimes. *Journal of Geophysical Research: Atmospheres*, 121(5), 2299–2317.  
754 doi: [10.1002/2015JD024502](https://doi.org/10.1002/2015JD024502)

755 Oreopoulos, L., N. Cho, D. Lee, M. Lebsock, and Z. Zhang, 2022: Assessment of two stochastic  
756 subcloud generators using observed fields of vertically resolved cloud extinction. *J. Atmos.*  
757 *Tech.*, 39, 1229-1244. <https://doi.org/10.1175/JTECH-D-21-0166.s1>

758 Palmer, M. D., D. J. McNeall, and N. J. Dunstone, 2011: Importance of the deep ocean for  
759 estimating decadal changes in Earth’s radiation balance. *Geophys. Res. Lett.*, 38, L13707.  
760 Doi:10.1029/2011GL047835

761 Paulot, F., Paynter, D., Ginoux, P., Naik, V., & Horowitz, L. W. (2018). Changes in the aerosol  
762 direct radiative forcing from 2001 to 2015: Observational constraints and regional  
763 mechanisms. *Atmospheric Chemistry and Physics*, 18(2018), 13265.  
764 <https://doi.org/10.5194/acp-18-13265-2018>

765 Quass, J., et al., 2022: Robust evidence for reversal in the aerosol effective climate forcing trend.  
766 *Atmos. Chem. Phys.*, <https://doi.org/10.5194/acp-2022-295>

767 Raghuraman, S. P., D. Paynter, and V. Ramaswamy, 2021: Anthropogenic forcing and response  
768 yield observed positive trend in Earth’s energy imbalance. *Nature. Comm.*,  
769 <https://doi.org/10.1038/s41467-021-24544-4>

770 Raghuraman, S. P., D. Paynter, R. Menzel, and V. Ramaswamy, 2023: Forcing, cloud feedbacks,  
771 cloud masking, and internal variability in the cloud radiative effect satellite record. *J.*  
772 *Climate*, 36, 4151-4167. <https://doi.org/10.1175/JCLI-D-22-0555.1>

773 Rienecker, M. M., and Coauthors, 2008: The GOES-5 Data Assimilation System—  
774 Documentation of versions 5.0.1, 5.1.0, and 5.2.0. NASA Tech. Rep. Series on Global  
775 Modeling and Data Assimilation, Vol. 27, NASA/TM-2008-105606, 97 pp.

776 Rossow, W. B., and R. A. Schiffer, 1991: ISCCP cloud data products. *Bull. Amer. Meteor. Soc.*,  
777 72, 2–20, [https://doi.org/10.1175/1520-0477\(1991\)072,0002:ICDP.2.0.CO;2](https://doi.org/10.1175/1520-0477(1991)072,0002:ICDP.2.0.CO;2).

778 Sassen, K., and Z. Wang, 2008: Classifying clouds around the globe with the CloudSat radar: 1-  
779 year of results. *Geophys. Res. Lett.*, 35, L04805, <https://doi.org/10.1029/2007GL032591>.

780 Schmidt, G. A., T. Andrews, S. E. Bauer, P. Durack, N. G. Loeb, V. Ramaswamy, et al., 2023:  
781 CERESMIP: a climate modeling protocol to investigate recent trends in the Earth's Energy  
782 Imbalance. *Front. Clim.*, 5, <https://doi.org/10.3389/fclim.2023.1202161>

783 Scott, R. C., T. A. Myers, J. R. Norris, M. D. Zelinka, S. A. Klein, M. Sun, D. R. Doelling, 2020:  
784 Observed Sensitivity of Low-Cloud Radiative Effects to Meteorological Perturbations over  
785 the Global Oceans. *J. Climate*, 33(18), 7717-7734. doi: 10.1175/JCLI-D-19-1028.1

786 Shankar, M., N. G. Loeb, N. Smith, N. Smith, J. L. Daniels, S. Thomas, and D. Walikainen,  
787 2023: Evaluating the radiometric performance of the Clouds and the Earth's Radiant Energy  
788 System (CERES) instruments on Terra and Aqua over 20 years. *IEEE Trans. Geosci. Rem,*  
789 *Sens.*, 61, <https://ieeexplore.ieee.org/document/10309194>

790 Smith, C. J., R. J. Kramer, G. Myhre, K. Alterskjær, W. Collins, A. Sima, O. Boucher, J.-L.  
791 Dufresne, et al., 2020: Effective radiative forcing and adjustments in CMIP6 models,  
792 *Atmos. Chem. Phys.*, 20, 9591–9618, <https://doi.org/10.5194/acp-20-9591-2020>.

793 Soden, B. J., I. M. Held, R. Colman, K. M. Shell, J. T. Kiehl, and C. A. Shields, 2008:  
794 Quantifying climate feedbacks using radiative kernels. *J. Climate*, 21, 3504-3520. DOI:  
795 10.1175/2007JCLI2110.1

796 Storto, A., and C. Yang, 2024: Acceleration of the ocean warming from 1961 to 2022 unveiled  
797 by large-ensemble reanalyses. *Nat. Comm.*, 15:545, [https://doi.org/10.1038/s41467-024-](https://doi.org/10.1038/s41467-024-44749-7)  
798 [44749-7](https://doi.org/10.1038/s41467-024-44749-7)

799 Stubenrauch, C., and Co-Authors, 2024: Lessons learned from the updated GEWEX Cloud  
800 Assessment database. *Surveys in Geophysics*, (Accepted, this collection).

801 Subba, T., M. M. Gogoi, B. Pathak, P. K. Bhuyan, and S. S. Babu, 2020: Recent trend in the  
802 global distribution of aerosol direct radiative forcing from satellite measurements. *Atmos.*  
803 *Sci. Lett.*, 21. doi: 10.1002/asl.975

804 Sun, M., D. R. Doelling, N. G. Loeb, R. C. Scott, J. Wilkins, L. T. Nguyen, P.  
805 Mlynczak, 2022: Clouds and the Earth's Radiant Energy System (CERES) FluxByCldTyp  
806 Edition 4 Data Product. *J. Atmos. Oceanic Technol.*, 39(3), 303-318. doi: [10.1175/JTECH-](https://doi.org/10.1175/JTECH-D-21-0029.1)  
807 [D-21-0029.1](https://doi.org/10.1175/JTECH-D-21-0029.1)

808 Szopa, S., et al., 2021: Short-Lived Climate Forcers, in: *Climate Change 2021: The Physical*  
809 *Science Basis. Contribution of Working Group I to the Sixth Assessment Report of the*  
810 *Intergovernmental Panel on Climate Change*, edited by Masson-Delmotte, V., Zhai, P.,  
811 Pirani, A., Connors, S., Péan, C., Berger, S., Caud, N., Chen, Y., Goldfarb, L., Gomis, M.,  
812 Huang, M., Leitzell, K., Lonnoy, E., Matthews, J., Maycock, T., Waterfield, T., Yelekçi, O.,  
813 Yu, R., and Zhou, B., chap. 6, Cambridge University Press, Cambridge, United Kingdom  
814 and New York, NY, USA, 2021.



815 Thorsen, T. J., S. Kato, N. G. Loeb, and F. G. Rose, 2018: Observation-based decomposition of  
816 radiative perturbations and radiative kernels. *J. Climate*, 31, 10039-10058. doi:  
817 10.1175/JCLI-D-18-0045.1

818 Trenberth, K. E., and J. T. Fasullo, 2009: Global warming due to increasing absorbed solar  
819 radiation. *Geophys. Res. Lett.*, 36, L07706, doi:10.1029/2009GL037527

820 Trenberth, K. E., and J. T. Fasullo, 2010: Simulation of present day and 21st century energy  
821 budgets of the southern oceans. *J. Climate*, 23, 440-454.

822 Trenberth, K. E., J. T. Fasullo, and M. Balmaseda, 2014: Earth's energy imbalance. *J. Climate*,  
823 27, 3129-3144. DOI: 10.1175/JCLI-D-13-00294.1.

824 Trenberth, K. E., 2015a: Has there been a hiatus? *Science*, 349, 691-692, DOI:  
825 10.1126/science.aac9225

826 Trenberth, K. E., Y. Zhang, J. T. Fasullo, and S. Taguchi, 2015b: Climate variability and  
827 relationships between top-of-atmosphere radiation and temperatures on Earth, *J. Geophys.*  
828 *Res. Atmos.*, 120, 3642–3659, doi:10.1002/2014JD022887

829 Vaughan, M., and Coauthors, 2009: Fully automated detection of cloud and aerosol layers in the  
830 CALIPSO lidar measurements. *J. Atmos. Oceanic Technol.*, 26, 2034–2050,  
831 <https://doi.org/10.1175/2009JTECHA1228.1>.

832 von Schuckmann, K., M. D. Palmer, K. E. Trenberth, A. Cazenave, D. Chambers, N.  
833 Champollion, J. Hansen, S. A. Josey, N. Loeb, P.-P. Mathieu, B. Meyssignac, and M. Wild,  
834 2016: An imperative to monitor Earth's energy imbalance, *Nat. Clim. Change*, 6, 138–144,  
835 <https://doi.org/10.1038/nclimate2876>.

836 von Schuckmann, K., et al., 2023: Heat stored in the Earth system 1960–2020: where does the  
837 energy go?, *Earth Syst. Sci. Data*, 15, 1675–1709, [https://doi.org/10.5194/essd-15-1675-](https://doi.org/10.5194/essd-15-1675-2023)  
838 2023.

839 Wall, C. J., J. R. Norris, A. Possner, D. T. McCoy, I. L. McCoy, and N. J. Lutsko, 2022:  
840 Assessing effective radiative forcing from aerosol-cloud interactions over the global ocean.  
841 *PNAS*, 119, <https://doi.org/10.1073/pnas.2210481119>

842 Wolter, K., and M. S. Timlin, 1998: Measuring the strength of ENSO events - how does 1997/98  
843 rank? *Weather*, **53**, 315-324. DOI: [10.1002/j.1477-8696.1998.tb06408.x](https://doi.org/10.1002/j.1477-8696.1998.tb06408.x)

844 Wood, R., and C. S. Bretherton, 2006: On the relationship between stratiform low cloud cover  
845 and lower-tropospheric stability. *J. Climate*, 19, 6425–6432,  
846 <https://doi.org/10.1175/JCLI3988.1>.

847  
848 Wood, R., 2012: Stratocumulus clouds. *Monthly Weather Review*, 140, 2373-2423.  
849 [doi:10.1175/MWR-D-11-00121.1](https://doi.org/10.1175/MWR-D-11-00121.1)

850  
851 Xu, K.-M., Y. Zhou, M. Sun, S. Kato, and Y. Hu, 2023: Observed cloud type-sorted cloud  
852 property and radiative flux changes with the degree of convective aggregation from CERES  
853 data. *Journal of Geophysical Research Atmospheres*, 128, e2023JD039152.

854  
855 Yuan, T., H. Song, R. Wood, C. Wang, L. Oreopoulos, S. E. Platnick, S. von Hippel, K. Meyer,  
856 S. Light, and E. Wilcox, 2022: Global reduction in ship-tracks from sulfur regulations for  
857 shipping fuel. *Sci. Advanc.*, 8, <https://doi.org/10.1126/sciadv.abn7988>

858  
859 Zelinka, M. D., T. A. Myers, D. T. McCoy, S. Po-Chedley, P. M. Caldwell, P. Ceppi, P., et al.,  
860 2020: Causes of higher climate sensitivity in CMIP6 models. *Geophysical*  
861 *Research Letters*, 47, e2019GL085782. <https://doi.org/10.1029/2019GL085782>.

862  
863 Zhao, B., Jiang, J. H., Gu, Y., Diner, D., Worden, J., Liou, K.-N., et al. (2017). Decadal-scale  
864 trends in regional aerosol particle properties and their linkage to emission changes.  
865 *Environmental Research Letters*, 2017(12), 054021.

866  
867 Zhao, M. et al., 2018: The GFDL Global Atmosphere and Land Model AM4.0/LM4.0: 1.  
868 Simulation characteristics with prescribed SSTs, *J. Adv. Modeling Earth Syst.* 10.3, 691–  
869 734. <https://doi.org/10.1002/2017MS001208>.

870  
871

872

**Tables**

873 Table 1 Definition of cloud classes used to assess influence of cloud changes on ASR.

Cloud Class	Cloud Top Pressure (hPa)	EIS (K)	Latitude Range
Stratocumulus (Sc)	> 680	> 5	60°S-60°N
Stratocumulus-to-Cumulus Transition (SCT)	> 680	0 – 5	60°S-60°N
Shallow Cumulus (Cu)	> 680	< 0	60°S-60°N
Middle	440 – 680	-	60°S-60°N
High	< 440	-	60°S-60°N
Polar	-	-	90°S-60°S; 60°N-90°N

874

875 Table 2 Local average and monthly anomaly standard deviation in coverage (fraction), SW and OLR TOA fluxes,  
876 and SST for clear-sky and the cloud classes in Table 1 for 07/2002–06/2022. A “local” average is  
877 determined from geodetic-weighted monthly averages of all 1°x1° regions in which a given cloud type is  
878 observed. Also provided is the coverage of each clear or cloud class over the entire globe. Here, SSTs are  
879 from the CERES SSF1deg Ed4.1 daily product.

	Local Fraction		SW TOA Flux		LW TOA Flux		SST		Global Fraction (%)
	(%)		(Wm <sup>-2</sup> )		(Wm <sup>-2</sup> )		(K)		
	Avg	Stdev	Avg	Stdev	Avg	Stdev	Avg	Std	
Clear	34.1	0.47	53.7	0.36	271.1	0.47	290.0	0.16	34.0
Sc	52.2	1.45	113.9	4.16	242.1	2.09	281.1	0.74	7.0
SCT	40.9	0.71	95.2	1.67	257.1	1.22	289.6	0.40	12.7
Cu	20.2	0.46	97.0	1.06	276.8	0.79	299.6	0.27	8.9
Middle	12.5	0.22	117.1	0.85	234.5	0.68	293.1	0.16	11.1
High	20.4	0.38	125.2	0.97	202.3	1.09	293.1	0.16	18.2
Polar	76.6	1.17	157.6	1.76	198.9	1.31	266.0	0.43	8.1

880  
881

882  
883  
884

Table 3 Average solar irradiance, ASR, -OLR and Net TOA radiation in  $\text{Wm}^{-2}$  for the first and most recent decades of CERES observations.

	Solar Irradiance	ASR	-OLR	NET
03/2000-02/2010	340.14	240.7	-240.2	0.53
01/2013-12/2022	340.16	241.6	-240.6	1.05
Difference	0.02	0.9	-0.4	0.52

885  
886

887 Table 4 Hemispheric and global trends in ASR, -OLR and NET for 03/2000–12/2022 in  $\text{Wm}^{-2}$  decade<sup>-1</sup>.

888 Uncertainties are given as 2.5–97.5% confidence intervals.

	SH	NH	Globe	SH minus NH
ASR	0.62±0.23	0.80±0.22	0.71±0.19	-0.18±0.36
-OLR	-0.20±0.21	-0.33±0.21	-0.26±0.19	0.13±0.29
NET	0.42±0.26	0.48±0.21	0.45±0.18	-0.06±0.31

889

890

891 Table 5 Global trends in all-sky, clear-sky and CRE from EBAF and FluxbyCldTyp in  $\text{Wm}^{-2} \text{decade}^{-1}$ . Trends  
 892 exceeding the 2.5-97.5 confidence interval are indicated in bold.

	03/2000-12/2022	07/2002-12/2022	
	EBAF All-Sky	EBAF All-Sky	FBCT All-Sky
-SW	<b>0.73±0.21</b>	<b>0.68±0.25</b>	<b>0.67±0.26</b>
-OLR	<b>-0.26±0.19</b>	<b>-0.25±0.22</b>	-0.20±0.30
NET	<b>0.45±0.18</b>	<b>0.47±0.21</b>	<b>0.50±0.23</b>
	EBAF Clear-Sky	EBAF Clear-Sky	FBCT Clear-Sky
-SW	<b>0.36±0.11</b>	<b>0.32±0.12</b>	<b>0.33±0.12</b>
-OLR	0.12±0.16	0.11±0.19	0.29±0.29
NET	<b>0.46±0.14</b>	<b>0.46±0.16</b>	<b>0.65±0.19</b>
	EBAF CRE	EBAF CRE	FBCT CRE
-SW	<b>0.37±0.18</b>	<b>0.36±0.22</b>	<b>0.34±0.20</b>
-OLR	<b>-0.38±0.09</b>	<b>-0.36±0.11</b>	<b>-0.49±0.10</b>
NET	-0.008±0.19	0.008±0.21	-0.15±0.20

893

894

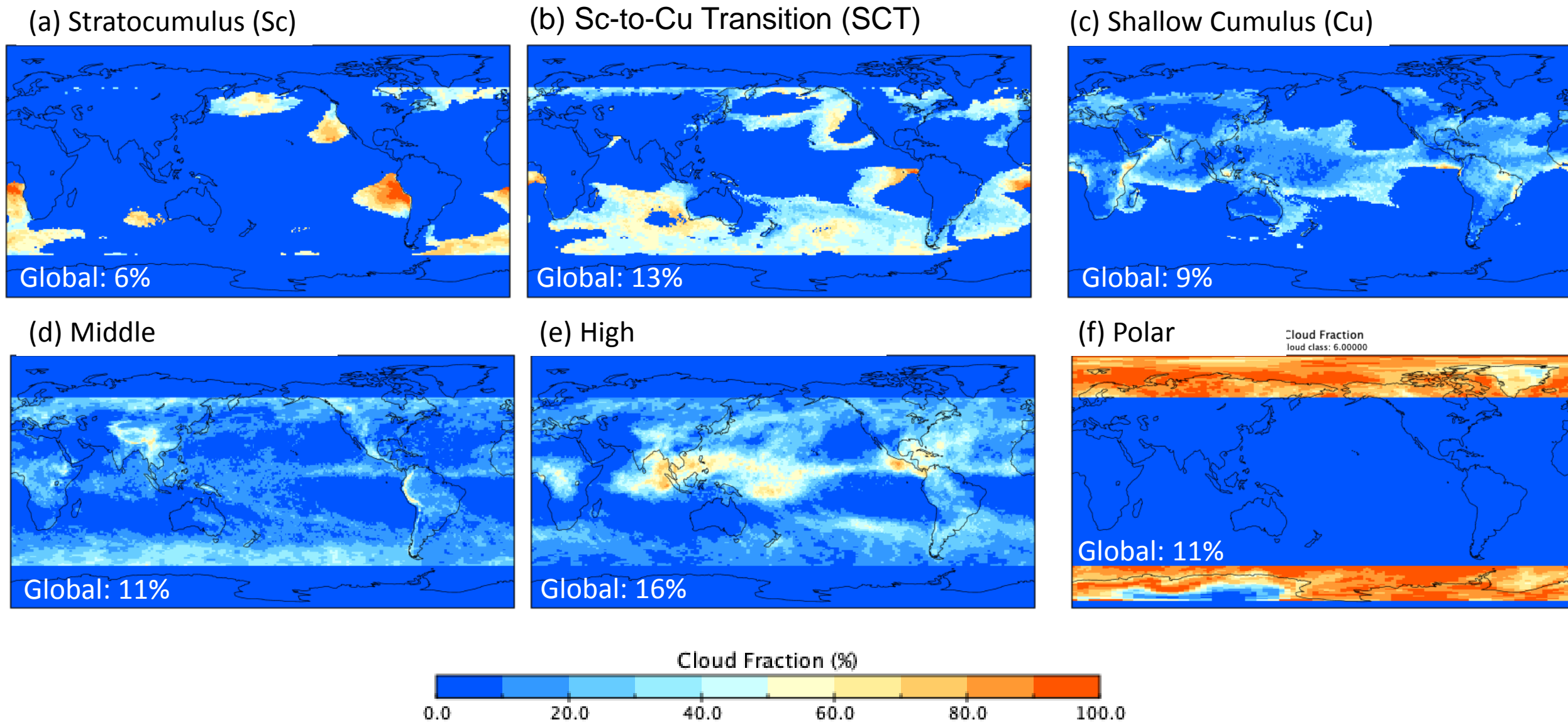


Figure 1 Cloud Fraction by Cloud Class for September 2002. Global coverages of each cloud class are as indicated.



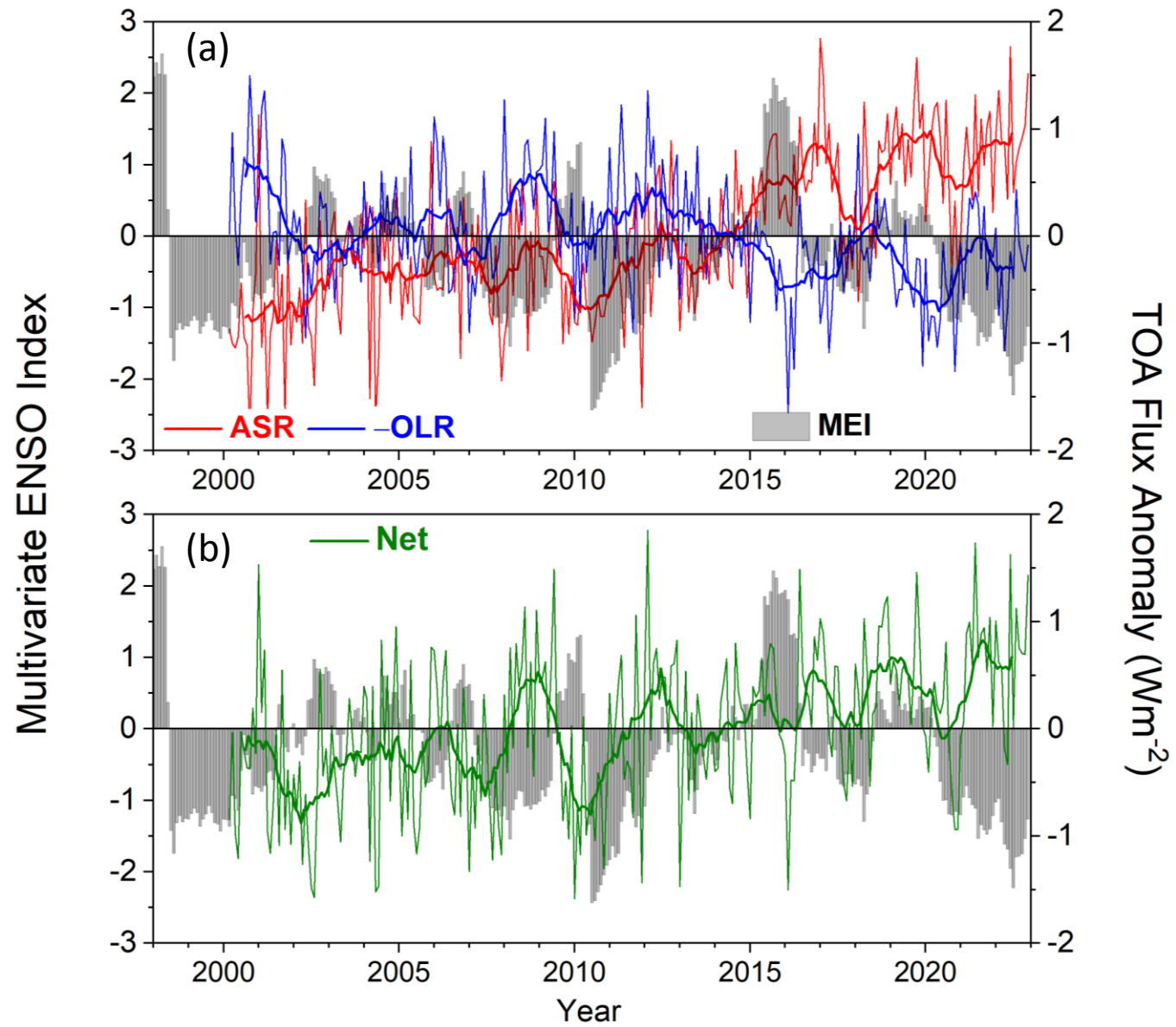


Figure 2 Global mean all-sky TOA flux anomalies and multivariate ENSO index from CERES EBAF Ed4.2 for 03/2000–12/2022. (a) ASR and -OLR; (b) NET.

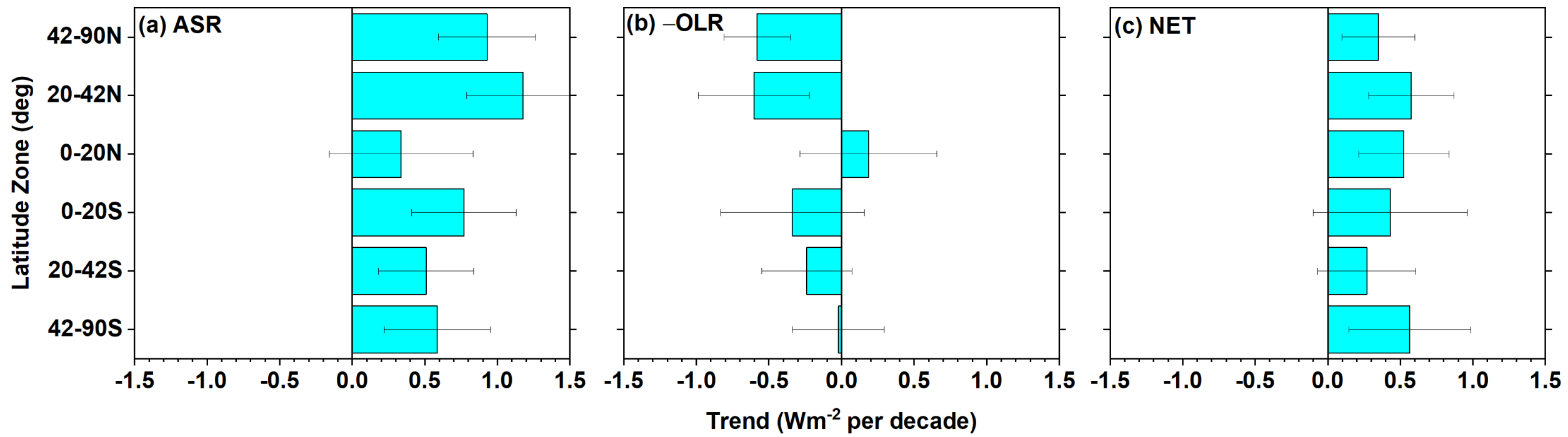


Figure 3 Zonal mean all-sky TOA flux trends for 03/2000–12/2022. (a) ASR; (b) -OLR; (c) NET.

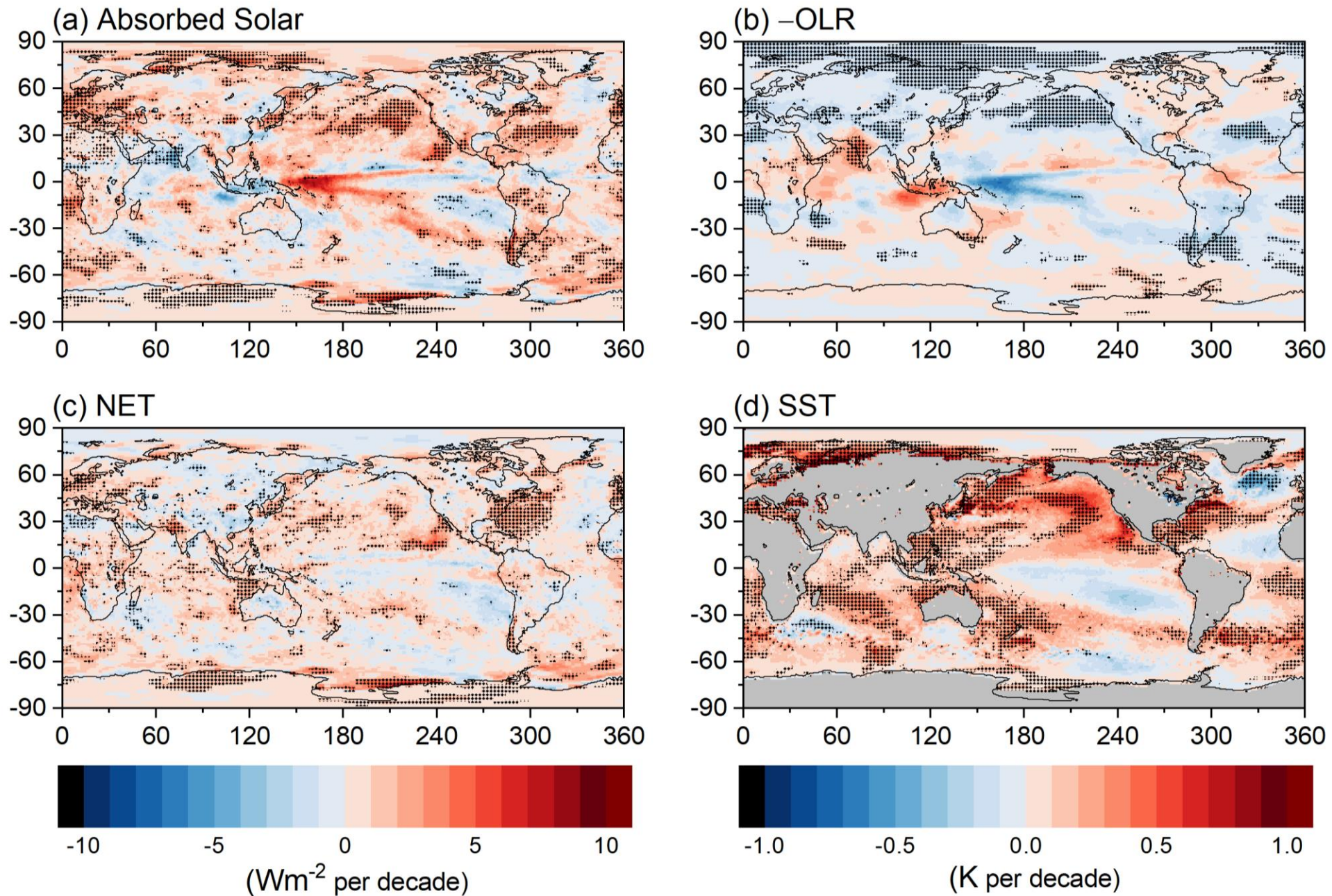


Figure 4 Regional trends in (a) ASR, (b) -OLR, (c) NET (Wm<sup>-2</sup> per decade), and (d) SST (K per decade) for 03/2000–12/2022. Hatching indicates trends significant at 2.5-97.5% confidence level. SSTs are from ECMWF Reanalysis 5 (ERA5) (Hersbach et al., 2020).

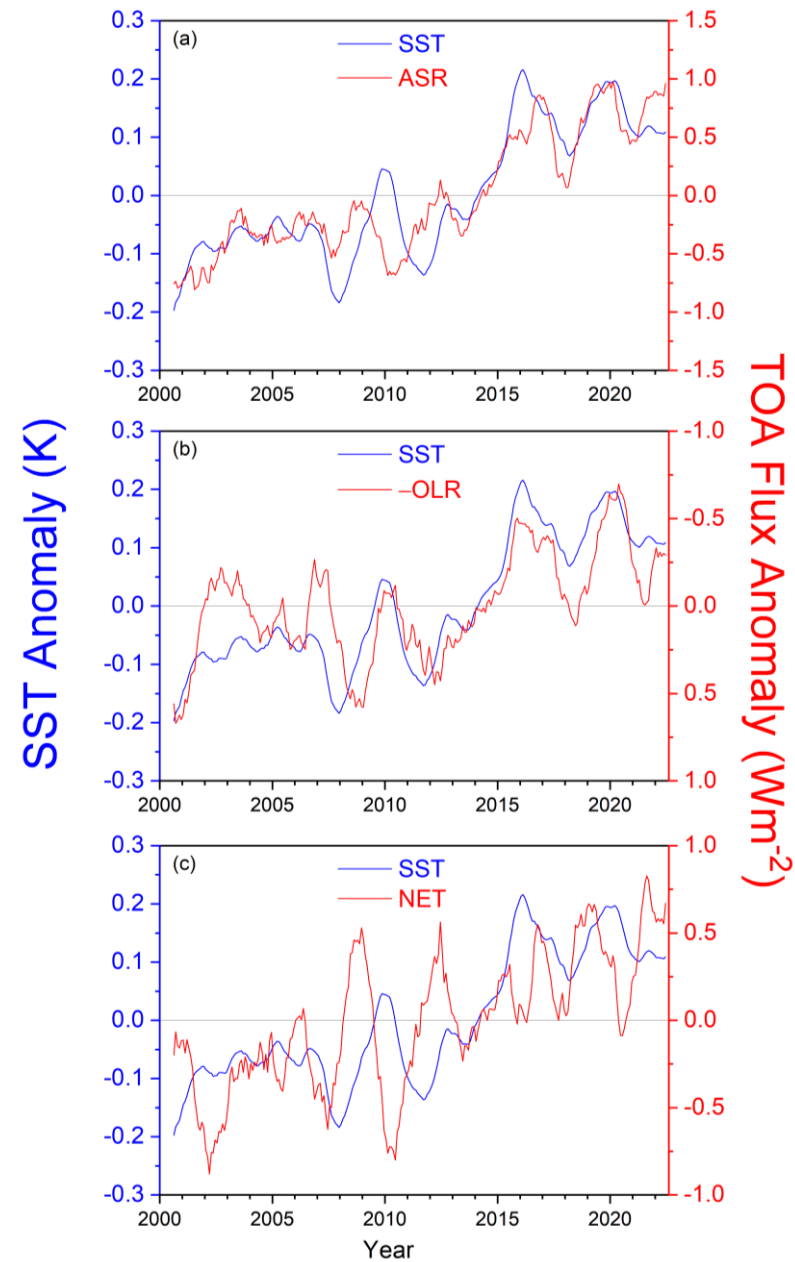


Figure 5 Twelve-month running average global anomalies in ERA5 SST and (a) ASR, (b) OLR (positive up), and (c) net TOA radiation. Period considered: 03/2000–12/2022.

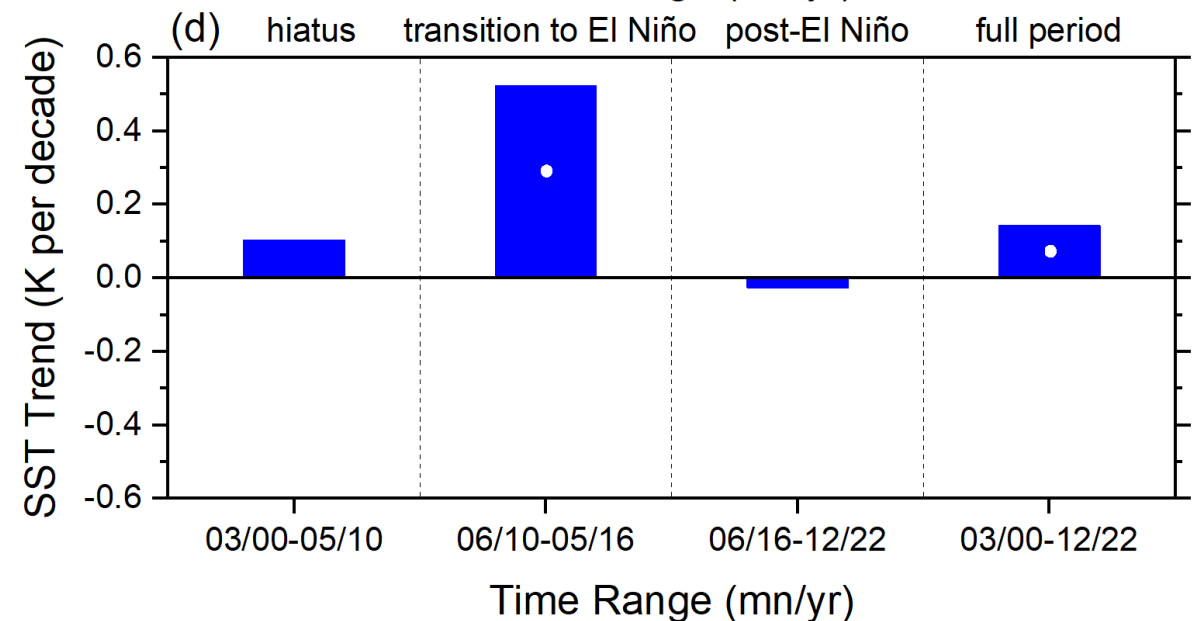
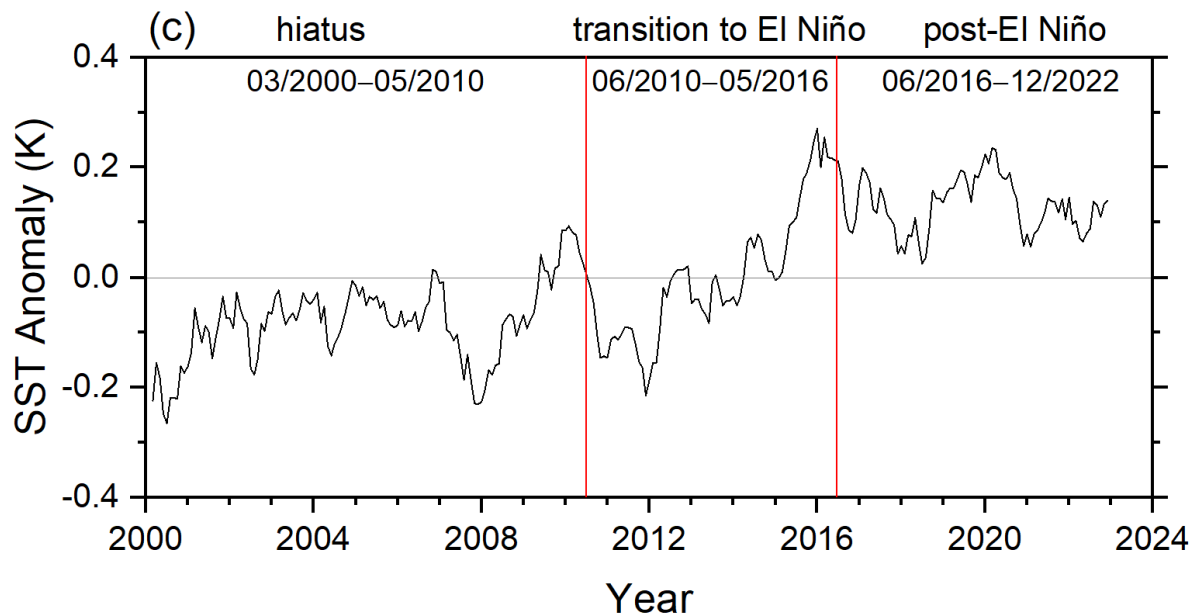
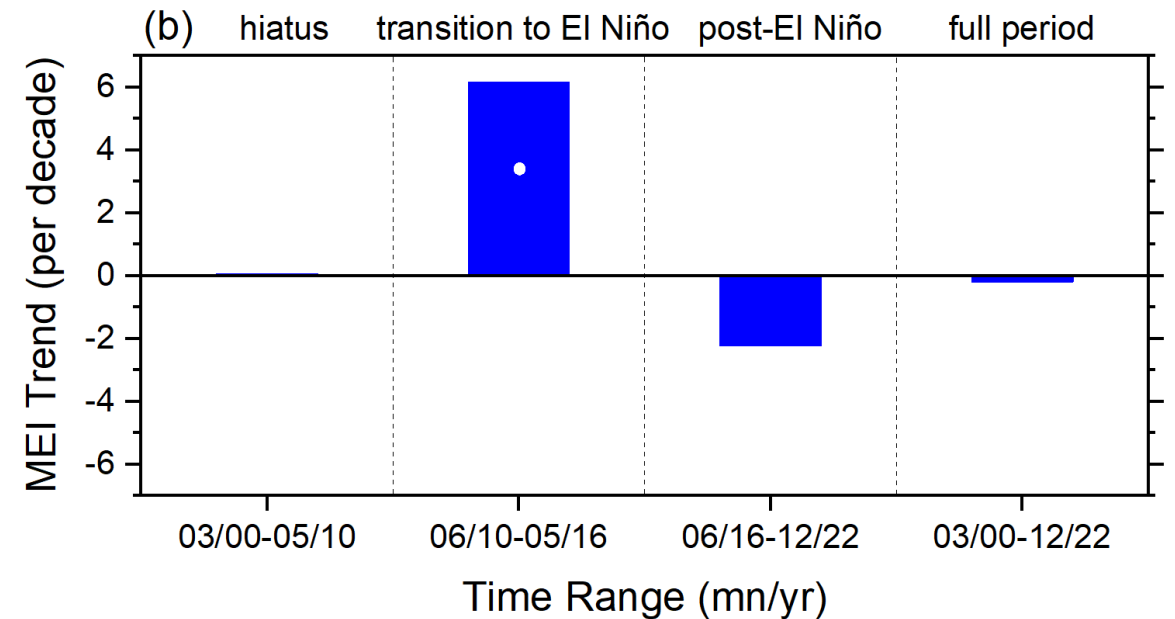
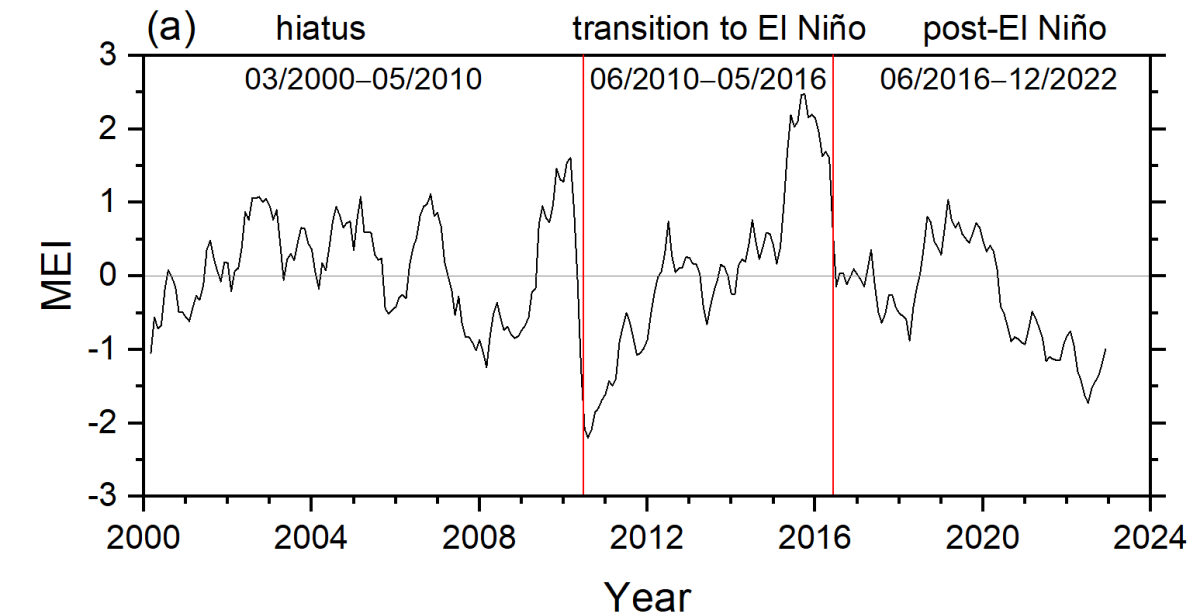


Figure 6 Monthly time series (a, c) and trends (b, d) for MEI (top) and anomalies in ERA5 SST (bottom). White circles in (b) and (d) correspond to trends that exceed the 2.5-97.5% CI. Time period 03/2000–12/2022.

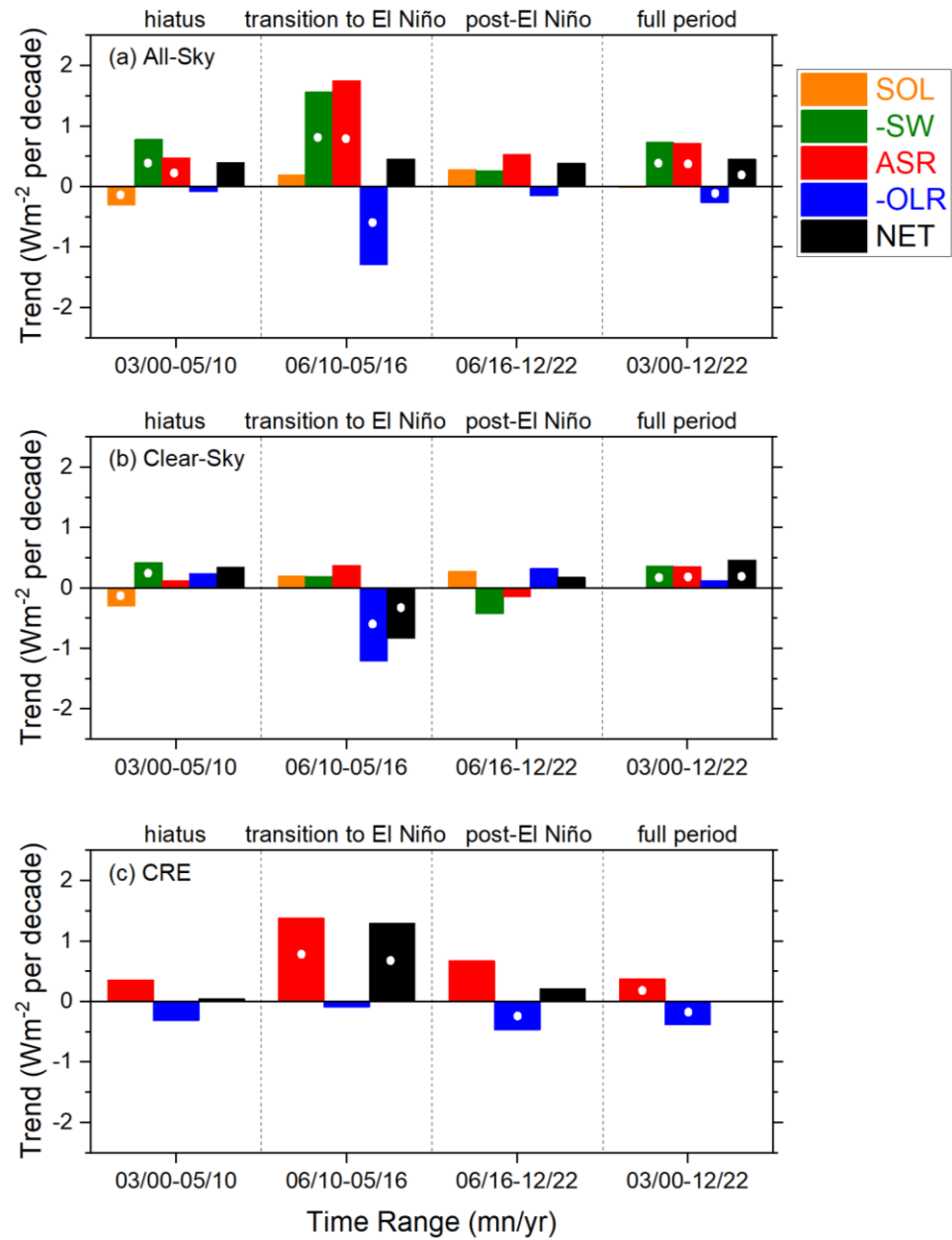


Figure 7 Trends in solar irradiance (SOL),  $-SW$ , ASR,  $-OLR$ , and NET TOA flux for (a) All-Sky, (b) Clear-Sky and (c) CRE. White circles indicate trends that exceed the 2.5-97.5% CI.

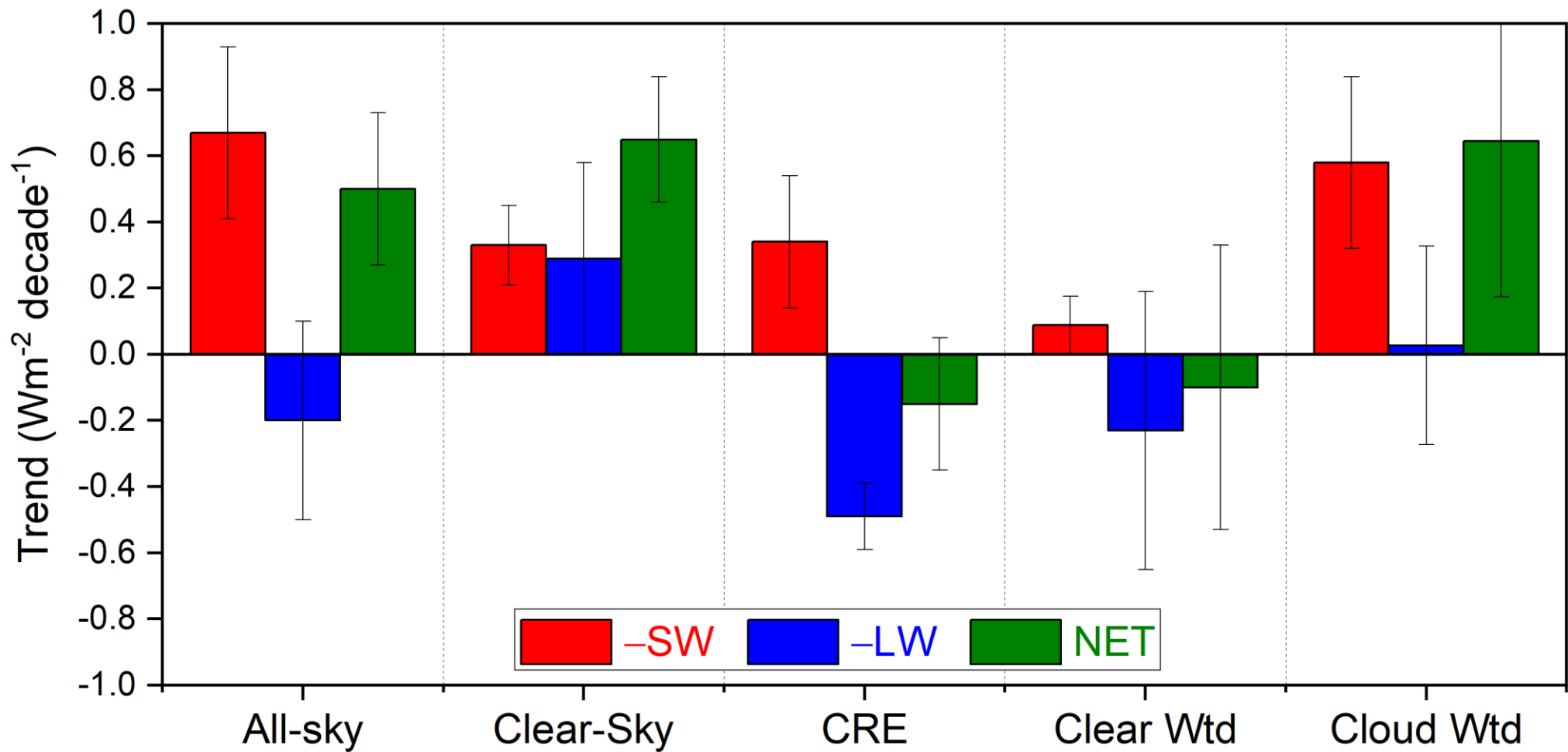


Figure 8 Trends in all-sky and clear-sky flux, CRE, clear fraction weighted clear-sky column (Clear Wtd) and cloud fraction weighted cloudy column (Cloud Wtd) flux contributions for  $-SW$ ,  $-OLR$ , and NET TOA flux from FBCT product. Error bars correspond to 2.5-97.5% CI. Time period: 07/2002-12/2022.

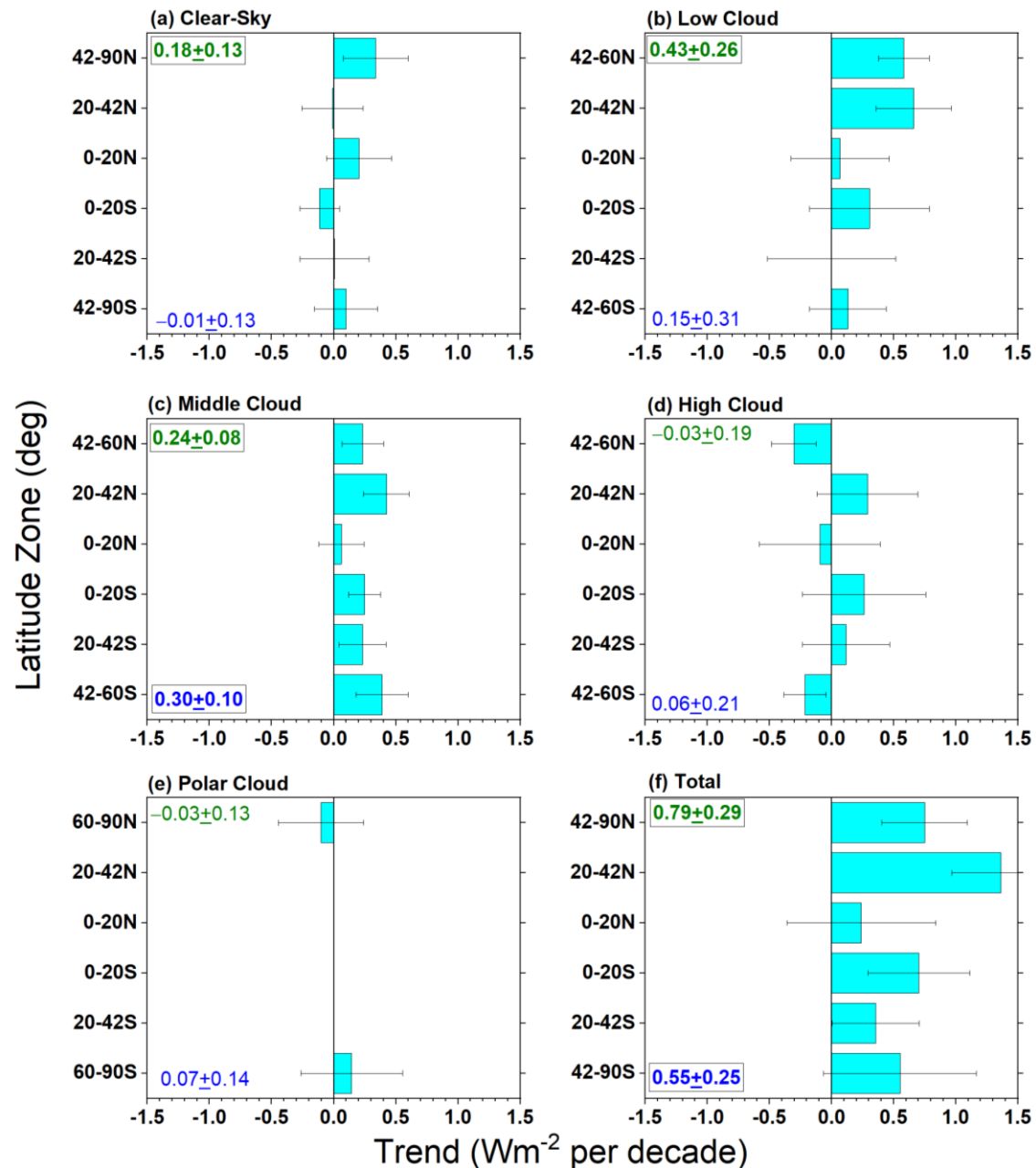


Figure 9 Contribution to zonal mean  $-SW$  trend from (a) clear-sky, (b) low cloud, (c) middle cloud, (d) high cloud, (e) polar cloud, (f) all. Period considered: 07/2002–12/2022. The SH and NH hemispheric average trends for each cloud type are indicated in each figure.



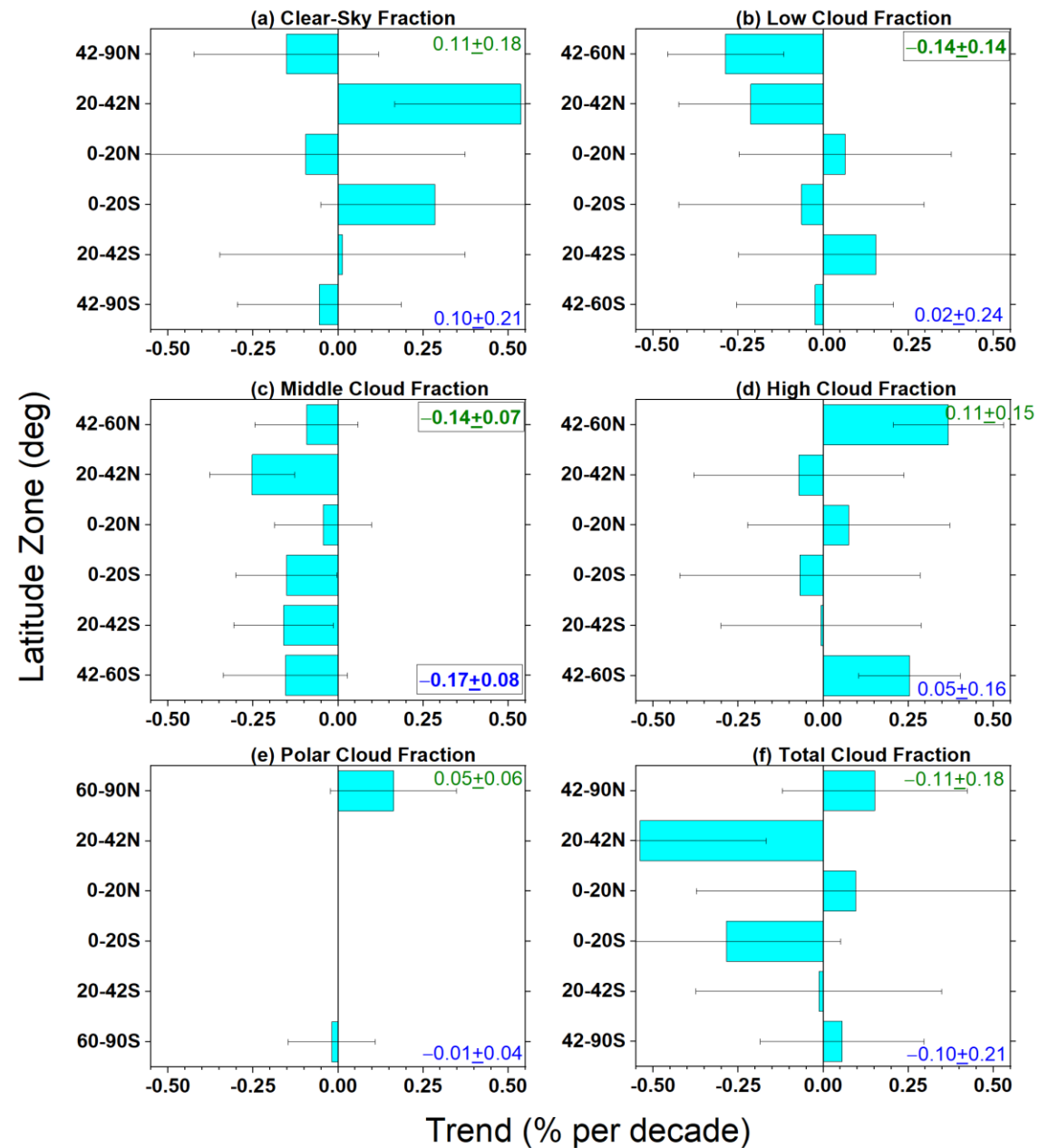


Figure 10 Same as Figure 9 but for clear-sky and cloud fraction.

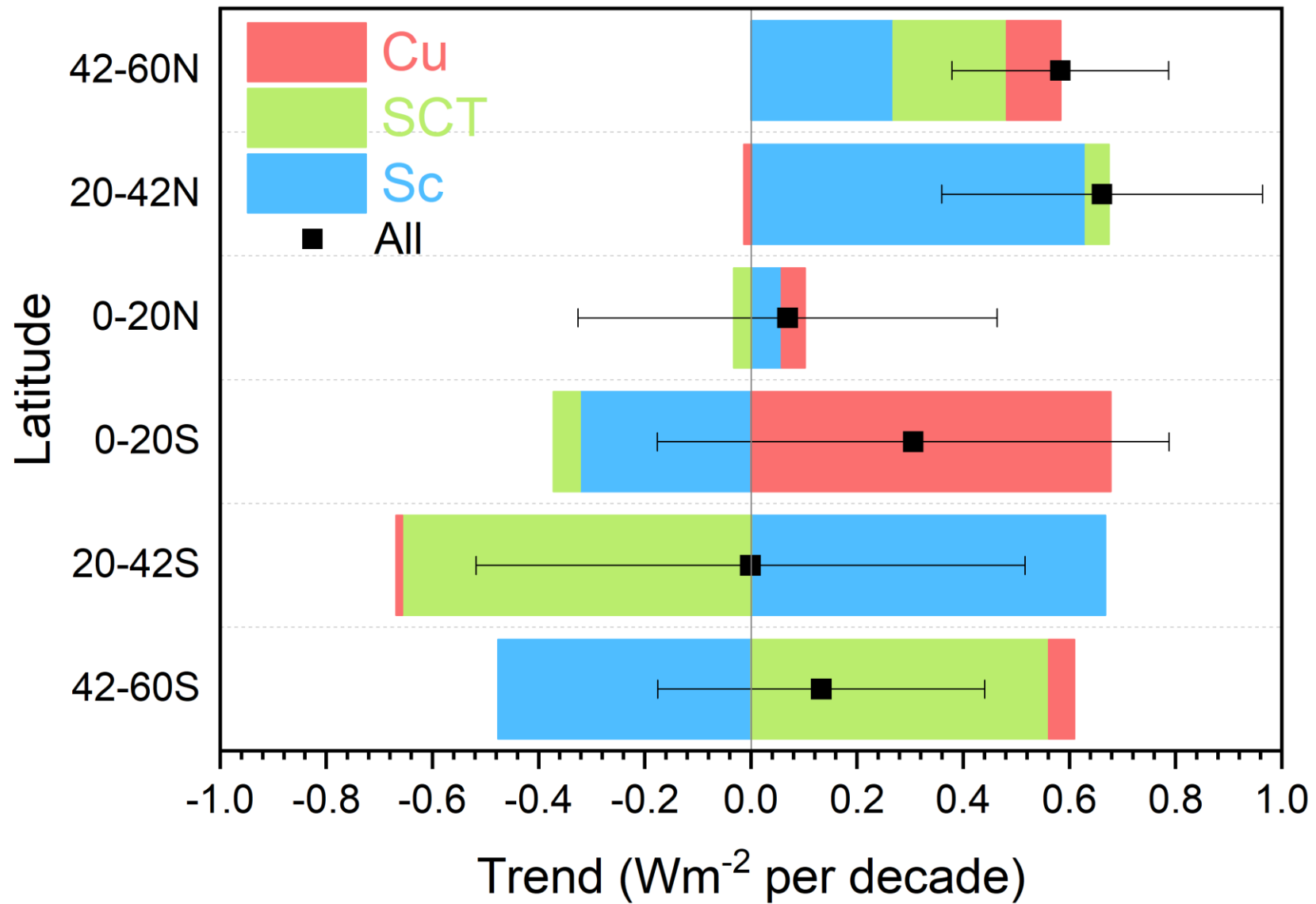


Figure 11 Zonal low cloud trends with contribution from Cu SCT and Sc. Period considered: 07/2002–12/2022.

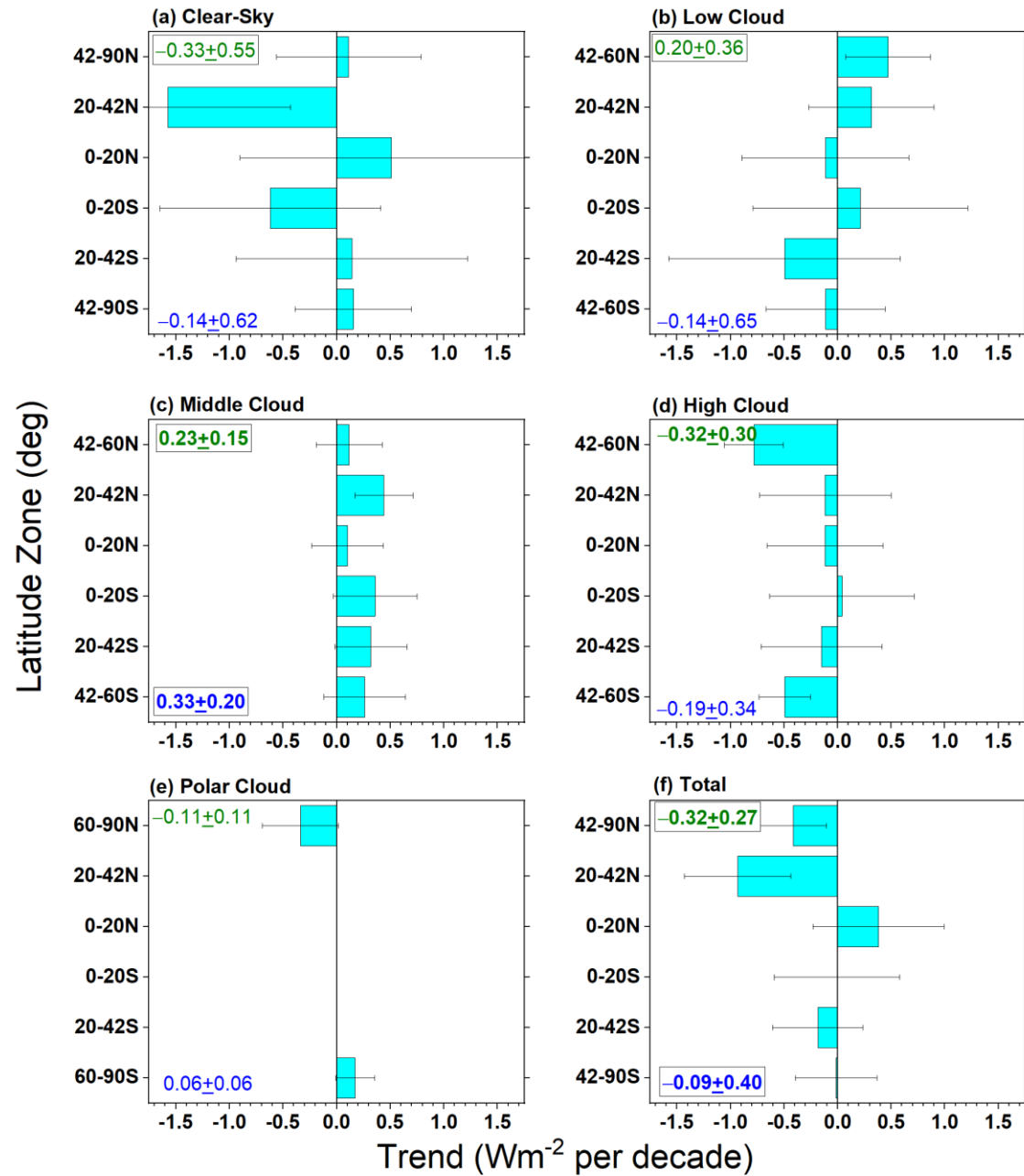


Figure 12 Same as Fig. 9 but for  $\square$ LW.

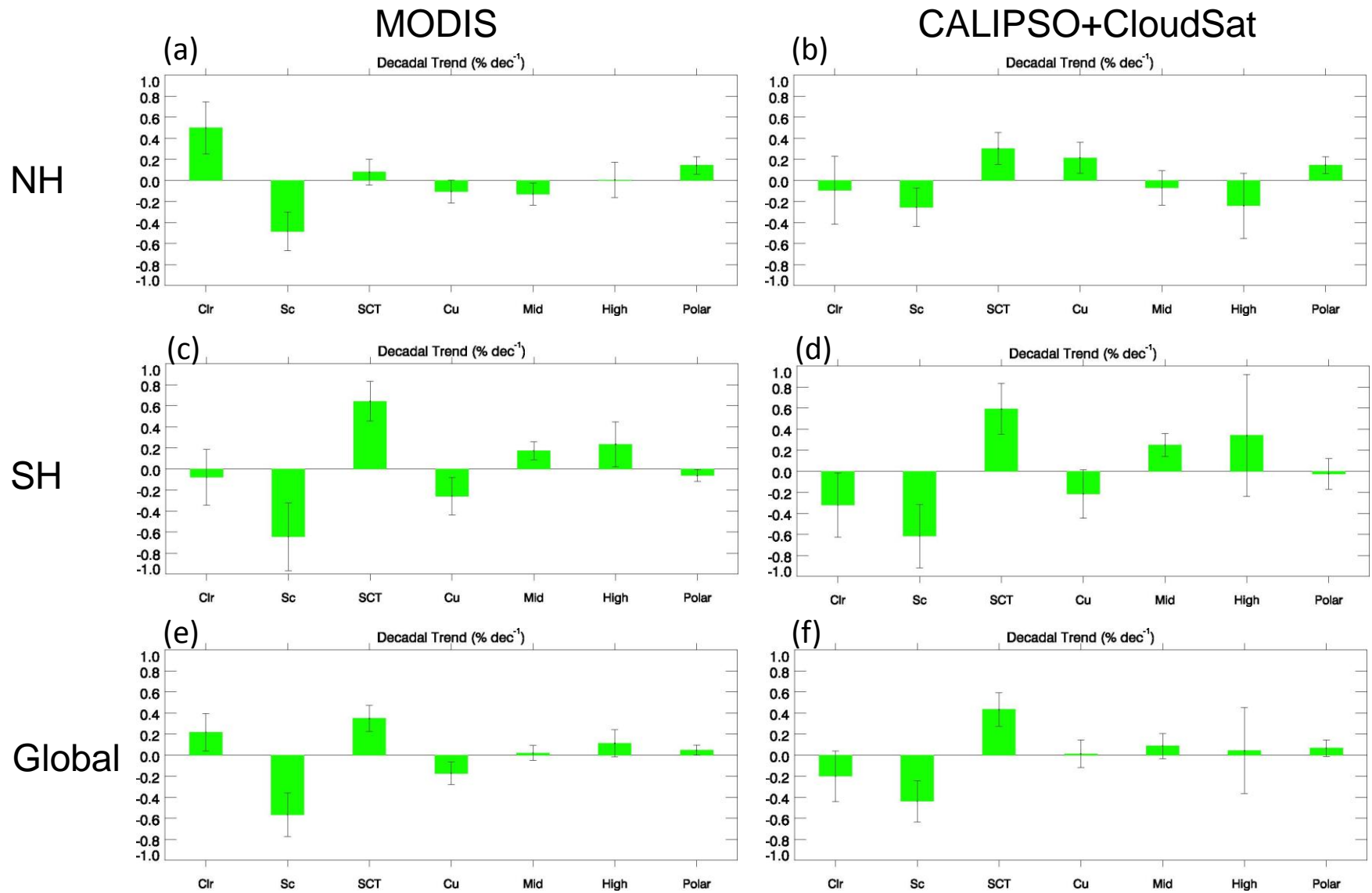


Figure 13 Clear-sky frequency and cloud fraction trends by cloud type from: (a) MODIS for NH, (b) CC for NH, (c) MODIS for SH, (d) CC for SH, (e) MODIS for globe, and (f) CC for globe using coincident measurements from 01/2008-12/2017.